Mitigation of Sea Ice Contamination in QuikSCAT Wind Retrieval

Weston Jay Hullinger

A thesis submitted to the faculty of
Brigham Young University
in partial fulfillment of the requirements for the degree of

Master of Science

David G. Long, Chair
Richard W. Christiansen
Gregory P. Nordin

Department of Electrical and Computer Engineering

Brigham Young University

April 2012

ABSTRACT

Mitigation of Sea Ice Contamination in QuikSCAT Wind Retrieval

Weston Jay Hullinger
Department of Electrical and Computer Engineering
Master of Science

Satellite borne radar scatterometers provide frequent estimates of near surface wind vectors over the Earth's oceans. However in the polar oceans, the presence of sea ice in or near the measurement footprint can adversely affect scatterometer measurements resulting in inaccurate wind estimates. Currently, such ice contamination is mitigated by discarding measurements within 50 km of detected sea ice. This approach is imperfect and causes loss of coverage. This thesis presents a new algorithm which detects ice-contaminated measurements based on a metric called the Ice Contribution Ratio (ICR) which measures the spatial ice contribution for each measurement. The ICR calculation is made for each measurement using a spatial ice probability map which is determined using Bayesian probability theory. Determined by simulation, the ICR processing thresholds the ICR for each measurement depending on local wind, ice backscatter, and cross-track location. ICR processing retrieves winds at a distance of 22.5 km from the ice edge on average, while ensuring wind accuracy. Retrieved wind distributions using ICR processing more closely resembles uncontaminated wind distributions than winds retrieved using previous methods. The algorithm is applied to QuikSCAT in this thesis but could be applied to other scatterometers such as the Oceansat-2 scatterometer.

ACKNOWLEDGMENTS

I express my gratitude to all those who who have helped me along my way as I have sought higher education. Such a list of people would spill onto many more pages than I have available. Thanks to family, friends, professors, colleagues, committee, scholarship donors, and more.

I give special thanks to my parents who have assured me that I can achieve any height that I desire. I am forever in their debt for their nurturing support and encouragement that has made it possible for me to be where I am. I further give thanks to my brothers and sisters for their encouragement as I have pushed myself to complete this thesis.

I acknowledge my greatest motivation for this thesis: that of my future family to which I wish to perpetuate the blessings that I have received.

To Dr. David G. Long, I give many thanks for being an expert teacher and mentor. He has taught me that the answers to problems are within myself and that I can access them with study and persistence.

My thanks also goes out to my friends in the Microwave Earth Remote Sensing Lab for their support and inspiration in solving unsolved problems. The value of collaboration with others could never be replaced by anything.

Table of Contents

x

List of Tables

List of Figures

Chapter 1

Introduction

Knowledge of polar winds is fundamental to understanding Earth's climate. Such winds influence atmospheric heat flow, ocean currents, and, possibly, sea-ice formation. Polar regions are, however, known for their inhospitality due to extreme weather, which makes on-site wind studies more difficult. Satellite remote sensing enables daily wind observations over the ocean in these regions.

Ocean wind speeds and directions can be measured using spaceborne radars called scatterometers. A scatterometer requires no sun illumination, penetrates the clouds, and can make measurements in the rain.

The Seawinds scatterometer on the QuikSCAT satellite has collected invaluable data regarding global climate from 1999 to 2009. The term QuikSCAT is commonly used for the scatterometer, too. QuikSCAT transmitted pulses at the Earth, measured the return power, and estimated the normalized radar cross section σ^0. QuikSCAT measured σ^0 from a polar orbit covering 90% of the Earth's surface daily. The orbit provided extensive coverage of the polar regions, enabling improved understanding of Arctic and Antarctic systems. Measured σ^0 values have long been used to estimate ocean wind vectors (wind retrieval). However, wind retrieval is not accurate if the σ^0 measurements are too close to land, icebergs, or sea ice.

1.1 Problem

Sea ice is a frequent contaminate of wind estimates in polar regions. The ice is constantly moving and typically has a radar signature similar to that of high wind speeds. As the radar takes measurements, its antenna pattern can illuminate both ocean and ice simul-

taneously. As a result, the ice's high radar signature may severely bias the σ^0 measurements, resulting in erroneous wind retrieval.

Previously, ice contaminated winds were eliminated by detecting the sea ice extent and then only estimating winds beyond a distance of 50 km from the ice. My analysis suggests that this method can still result in ice contamination and also eliminates many valid estimates that could be retained.

1.2 Approach

Here I propose a new algorithm for detecting ice contaminated QuikSCAT measurements in order to discard them before wind retrieval. Thus winds are only retrieved from uncontaminated measurements increasing wind estimate accuracy. In addition, the algorithm retrieves valid wind estimates closer to the ice edge than before possible.

A successful land contamination mitigation technique has been developed by Owen and Long [1]. The algorithm measures a ratio of how much of the antenna pattern overlaps land and equates that to wind error. Land-contaminated measurements that can be expected to result in high wind error are discarded prior to wind retrieval. The algorithm in this thesis is inspired by this work with significant modifications to deal with the variability in sea ice movement from day to day. Sea ice has been known to drift almost 80 km in a single day [2,3].

In this thesis, a metric for ice contamination detection is introduced: the Ice Contribution Ratio (ICR). The ICR calculation depends on the estimated spatial probability of sea ice. The ICR relates to σ^0 measurements through a model developed here. This model is used to estimate the wind error for different ICR values. ICR thresholds are determined to achieve acceptable wind error. Measurements are discarded when their ICRs are above the ICR threshold. Wind retrieval performed using the remaining measurements is ensured to be more accurate. This algorithm mitigates ice contamination more successfully than previous methods while retrieving winds 22.5 km from the ice edge on average. The principle components and results of this thesis have been submitted for publication.

1.3 Outline

This thesis presents the ice contamination mitigation algorithm in detail. Chapter 2 is a background which covers scatterometry, QuikSCAT, low and high resolution products, wind retrieval, and ice contamination. Chapter 3 outlines the Ice Contribution Ratio (ICR) metric and its algorithm for contaminated measurement detection using Bayesian probability theory. Chapter 4 presents case study results in the Antarctic and Arctic oceans as well as long term quantitative algorithm performance analysis. Finally, Chapter 5 concludes with thesis contributions and future research.

Chapter 2

Background

2.1 Scatterometry

Scatterometry is a form of active remote sensing which is employed in estimating wind speeds from a satellite craft. The scatterometer sends out microwave pulses and then listens for and measures the echo power. A noise measurement is also generally taken and subtracted from the echo power to estimate the signal power received. Then the normalized radar cross section (σ^0) is calculated using the radar equation

$$\sigma^0 = \frac{(4\pi)^3 R^4 L P_s}{P_t G^2 \lambda^2 A},$$

(2.1)

where R is the range to the surface, L is the contribution from known system losses, P_s is the signal power received, P_t is the transmitted power, G is the antenna gain, λ is the wavelength at the center frequency of the transmitted signal, and A is the effective illuminated area.

The quantity P_s, and therefore σ^0, is a function of measurement geometry and target surface properties. The radar cross section generally decreases as the incidence angle increases. Different azimuth angles can also change σ^0 depending on the surface target shape and periodicity. Additionally, the dielectric properties of the target contribute because the incident wave creates surface currents that retransmits the return signal. Finally, surface roughness also contributes significantly.

A specular surface (smooth) reflects much of the signal at opposite its incidence angle. However, if the surface is rougher the microwaves scatter in more directions. Most scatterometers employed in measuring wind vectors have off-nadir orientation, meaning that they do not point strait down at the earth. In an off-nadir configuration, a specular surface reflects much of the power away from the radar resulting in a low σ^0. As the surface roughness

increases, more signal scatters in other directions, therefore causing more to return to the radar antenna. Thus, a rough surface has higher σ^0 than a specular surface.

2.2 QuikSCAT

QuikSCAT executed its mission from June 19, 1999 to November 23, 2009. Although the mission is over, its measurements provided valuable information about Earth's environment, so much so, that another, similar scatterometer started its mission aboard Oceansat-2 on November 4, 2009 giving data continuation [4]. While this study is applied to QuikSCAT, the ICR algorithm can also be applied to Oceansat-2 data.

Measurements from QuikSCAT have been employed to study many of the Earth's geophysical systems. The original mission objective was to estimate ocean surface wind vectors. Additionally QuikSCAT's polar orbit enables extremely high coverage in polar regions. This has enabled iceberg tracking, sea ice mapping, and snow studies.

QuikSCAT transmits and receives pulses at 13.4 GHz with a dual polarized pencil beam antenna system. Its horizontally-polarized (Hppl) inner beam and vertically-polarized (Vpol) outer beam point at 46 and 54 degree incidence angles respectively as illustrated in Figure 2.1. The two beams rotate as the satellite moves along its nadir track (or along track) covering a 1600 km wide swath. The swath direction orthogonal to the nadir track is the cross track direction. Using this configuration, QuikSCAT collects forward and aft looking measurements for both polarizations with the exception of the outer edges of the swath in the cross track direction. This small swath region is called the outer swath and produces only Vpol measurements.

An observed measurement σ^0_{Obs} can be modeled with noise according to

$$\sigma^o_{\text{Obs}} = \sigma^o_{\text{True}}(1 + K_p\eta),\tag{2.2}$$

where $\eta \sim \mathcal{N}(0,1)$ demonstrates multiplicative noise and K_p depends on measurement parameters such as SNR and geometry [5]. The quantity σ^0_{True} is the measurement without noise.
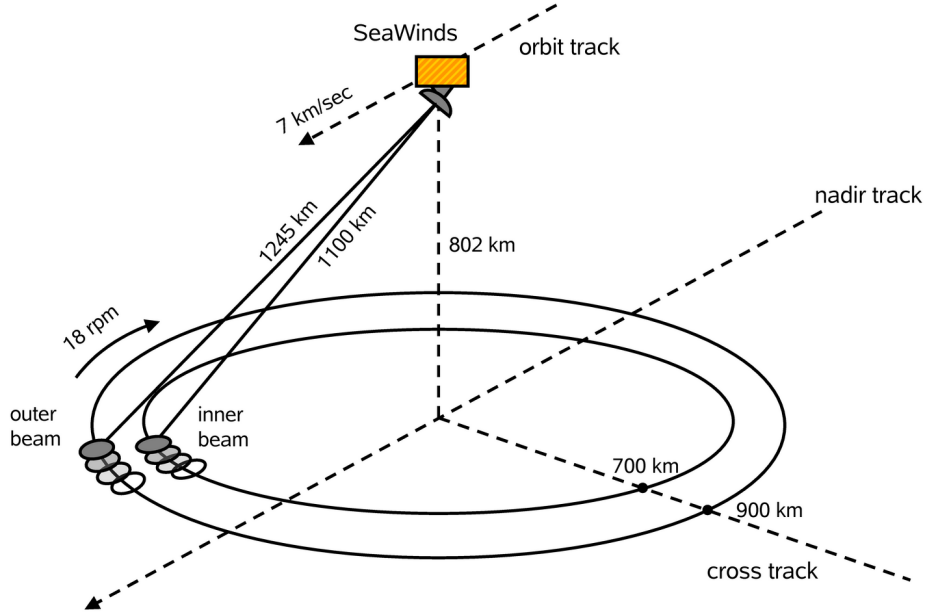
Figure 2.1: Geometry of the SeaWinds scatterometer aboard the QuikSCAT satellite.

Each σ_{True}^0 is a weighted average of a distributed σ^0 on the Earth's surface. The weighting function is called the spatial response function, $R(\mathbf{v})$, and is due to the antenna pattern's normalized projection onto the ground combined with signal processing [6]. The weighting function $R(\mathbf{v})$ averages the spatially distributed $\sigma^0(\mathbf{v})$ according to

$$\sigma_{\text{True}}^0 = \frac{\displaystyle\int_{\text{footprint}} \sigma^0(\mathbf{v}) R(\mathbf{v}) d\mathbf{v}}{\displaystyle\int_{\text{footprint}} R(\mathbf{v}) d\mathbf{v}}, \tag{2.3}$$

where $\mathbf{v}$ is the position vector of the location on the ground.

2.3 Low and High Resolution Products

The measurements which result from the full footprint spatial response are referred to as "egg" measurements. Egg measurements are used in the conventional 25 km resolution L2B wind data product reported by the Jet Propulsion Laboratory (JPL) [7].

Each egg measurement is made up of several smaller "slice" measurements collected using range/Doppler filtering. Researchers have derived and tabulated the slice spatial response function for QuikSCAT as seen in Figure 2.2 [5, 6]. Notice that the function reduces much more slowly in the direction of the major axis. This non-symmetry illustrates one reason why a simple distance metric is not sufficient to quantify contamination because the direction of the major axis varies with the antenna rotation angle. Using this response function and image reconstruction algorithms, researchers produce high resolution (HR) wind products [8, 9].
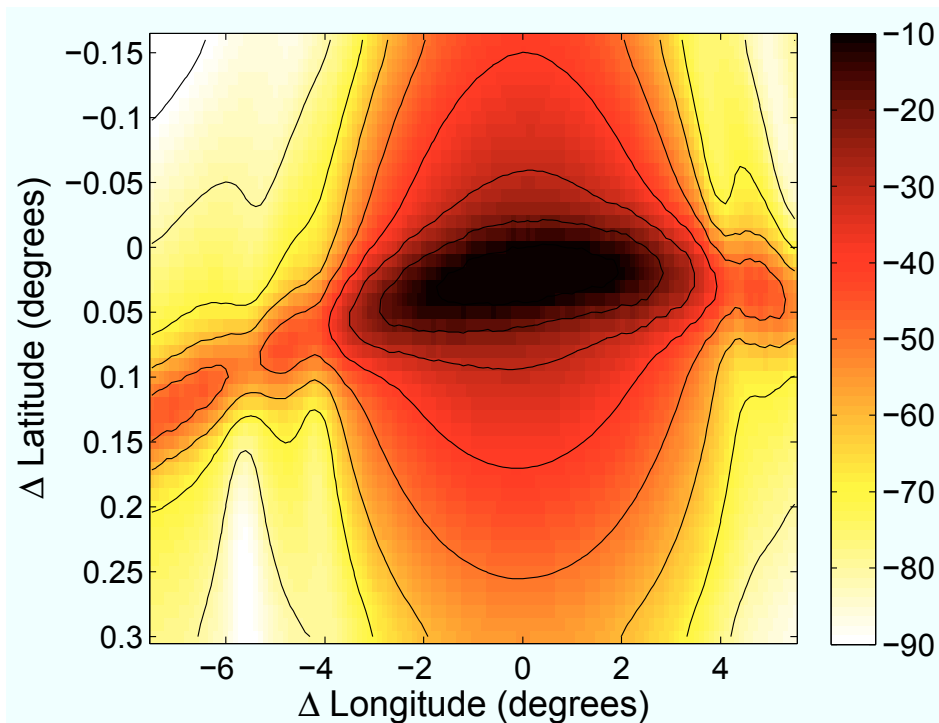
Figure 2.2: A sample slice spatial response function for QuikSCAT in dB. Contours are spaced 10 dB apart. The major axis is in the near horizontal direction and the minor axis is perpendicular.

Both conventional and HR wind products are grided in the along-track/cross-track directions. Each pixel is termed a wind vector cell (WVC) with 25 km resolution for conventional products and 2.5 km for HR. The WVC index in the direction of flight is termed the along track index. The index across the flight track is termed the cross track index.

Before HR wind retrieval is performed, the σ^0 measurements are averaged into WVC's using the AVE algorithm. The AVE algorithm enhances the data resolution from a single pass [10]. Azimuth diversity for wind retrieval requires that σ^0 measurements are sorted into 4 types: v-pol fore and aft, and h-pol fore and aft. Each WVC contains an average value for each type. The exception occurs on the swath's outer edge where only v-pol measurements are available. Wind is retrieved for each WVC as described in Section 2.4. The trade off for higher resolution is increased noise. Figure 2.3 shows an example of both the conventional L2B wind product and the HR wind product.

(a) Conventional L2B Wind Product   (b) High Resolution Wind Product
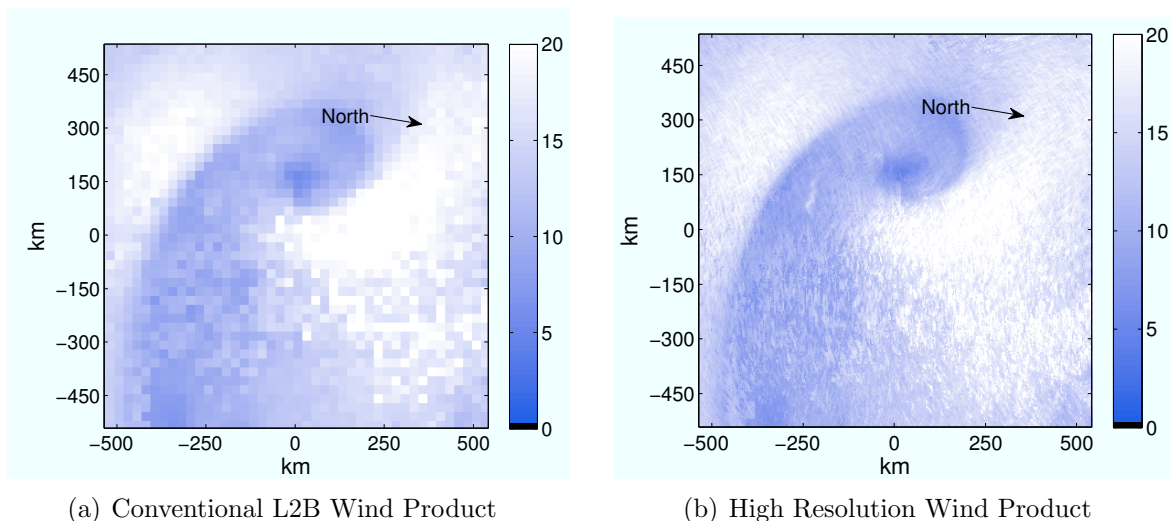
Figure 2.3: QuikSCAT wind speed products (m/s) at the L2B 25 km resolution and the High Resolution 2.5 km resolution. These products are of the Antarctic Ocean on December 25, 2004. The axis represent distances from 53.3 degrees South and 18.3 degrees East.

Another high resolution product used in this study is the scatterometer image recon-struction (SIR) image. The SIR algorithm [10,11] creates these images by applying irregular sampling theory to the plenitude of measurements taken by QuikSCAT from its several daily revolutions. Using several daily revolutions increases spatial resolution in exchange for loss of temporal resolution. The SIR algorithm also requires the measurement spatial response function. This enables production of high resolution σ^0 images of sea ice in Arctic and Antarctic regions from QuikSCAT σ^0 measurements. These images are created for Vpol as

seen in Figure 2.4(a) as well as for Hpol. Using Vpol, Hpol, and other SIR images, diurnal ice extent products are made by the Remund-Long (RL) algorithm [12, 13]. The RL algorithm uses an iterative maximum likelihood classifier as well as image processing techniques to produce daily sea ice extent maps. Examples of Antarctic SIR and RL ice map images are shown in Figure 2.4(b). These ice maps are used in producing the L2B wind product. The L2B product retrieves winds no closer than 50 km from the RL ice edge. The RL ice maps are also used as inputs to the ICR algorithm described in this thesis.

(a) QuikSCAT Vpol σ^0 SIR   (b) QuikSCAT RL Ice Map
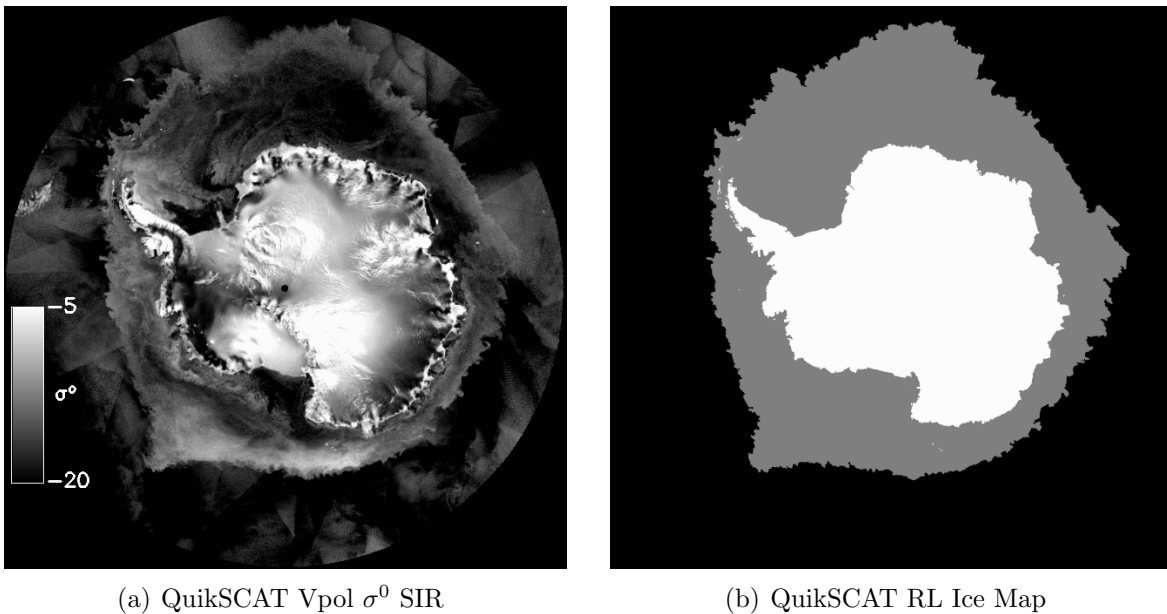
Figure 2.4: QuikSCAT Vpol σ^0 SIR and RL ice map images for Antarctic on August 30, 2009. a) The Vpol σ^0 SIR image is produced using the Scatterometer Reconstruction Algorithm developed at BYU. b) The RL ice map takes values of 0 for ocean, 1 for ice, and 2 for land.

2.4   Wind Retrieval

Wind retrieval is the process of transforming σ^0 measurements into wind vectors. Wind retrieval relies on a geophysical model function (GMF) [14–16] relating the near surface winds and particular observation geometry (incidence and azimuth angles) with σ^0. Various GMFs have been developed for QuikSCAT's frequency band, one of which is QMOD4 [7]

which is designed to better represent low and high wind. Figure 2.5 demonstrates the QMOD4 relationship between wind vectors and σ^0 for an incidence angle of 46 degrees. The relative azimuth angle is the azimuth angle measured from facing directly into the wind. Since the absolute azimuth angle (with respect to North) is known, the relative azimuth angle is all that is required to know the wind direction.
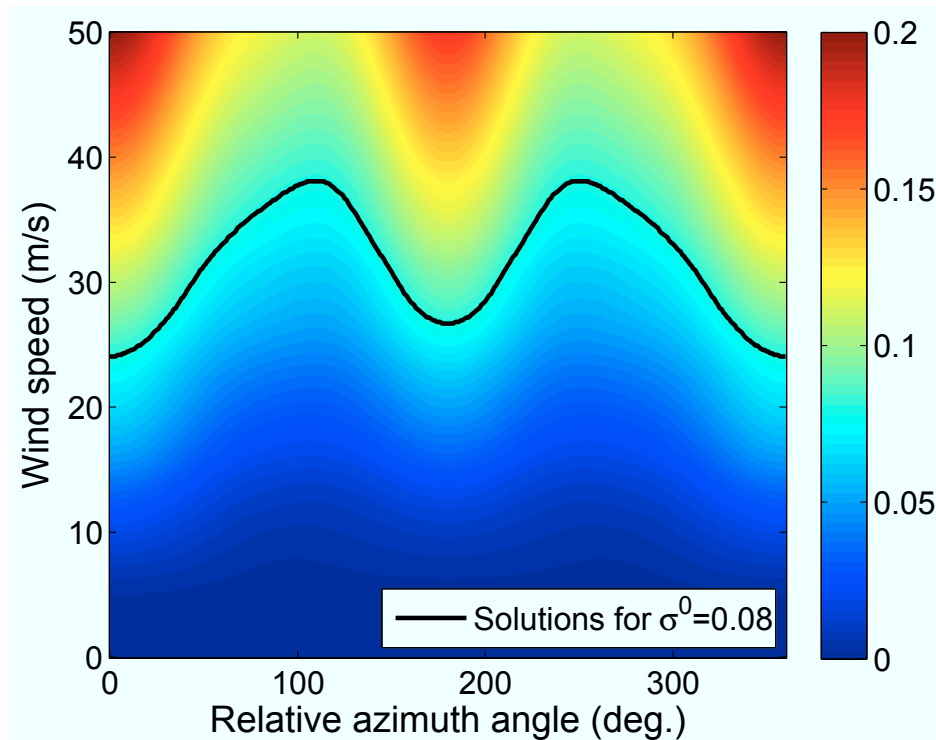
Figure 2.5: Geophysical model function for QuikSCAT at an incidence angle of 46 degrees. The relative azimuth angle is the measurement angle with respect to facing into the wind. The black line represents the possible solutions given σ^0 is 0.08.

Notice in Figure 2.5 that as the σ^0 increases with wind speed. When the wind speeds are low, the ocean surface is smooth and most microwave energy is reflected away from the antenna. When the wind speeds are higher, the surface is rougher resulting in more Bragg scattering back to the radar.

While the GMF computes σ^0 for a given azimuth angle and a wind speed, the inverse problem is less simple. When a measurement is taken, only the absolute azimuth angle is known. The relative azimuth angle is unknown, meaning that for a single σ^0 measurement

11

there is an entire curve of solutions for wind speed and direction. For the σ^0 measurement 0.08, Figure 2.5 shows the possible speed/direction solutions. Since the curve includes all relative azimuth angles, there is no information about the wind direction. The distance from the peak to trough gives only a coarse estimate of the speed. This is overcome by taking measurements from multiple absolute azimuth directions and finding where the curves intersect. QuikSCAT's rotating beams collect measurements from multiple azimuth angles to solve this problem.

Wind retrieval methods include a maximum likelihood approach [9,17] and alternative methods such as the manifold approach [18]. In this thesis, wind vectors are estimated using a Gaussian noise model and maximum likelihood estimator. The probability density function (PDF) of an observed σ^0 given a true surface backscatter σ_t^o is often modeled as

$$p(\sigma^o|\sigma_t^o) = \frac{1}{\sqrt{2\pi\zeta^2}} \exp\left(-\frac{(\sigma^o - \sigma_t^o)^2}{2\zeta^2}\right), \tag{2.4}$$

where ζ^2 is the observation noise variance [19]. The uncorrelated amplifier noise dominates the observation noise, resulting in independence between the various measurements within a WVC. With this assumption in place, a likelihood function is derived as

$$l(\sigma^{\mathbf{o}}|\mathbf{w}) = -\sum_{i=0}^{k} \left(\ln(\zeta_i) + \frac{1}{2}\frac{(\sigma_i^o - \mathcal{M}(\mathbf{w}))^2}{\zeta_i^2}\right), \tag{2.5}$$

given a vector of observations, $\sigma^{\mathbf{o}}$, where $\mathcal{M}(\mathbf{w})$ is the GMF which maps $\mathbf{w}$ to $\sigma_{t,i}^o$ given the geometry for σ_i^o in the vector $\sigma^{\mathbf{o}}$. The index i indicates the measurement of the total k measurements contributing to the wind estimate. Therefore ζ_i^2 refers to the noise variance for the observation σ_i^o. Wind is retrieved by choosing $\mathbf{w}$ to maximize likelihood function

For QuikSCAT wind retrieval, the likelihood function generally has up to four maximums associated with possible wind solutions, which are called ambiguities. Although these ambiguities are generally similar in magnitude, they can differ significantly in direction. Although several ambiguity selection methods exist, a reasonably successful method involves applying an iterative median filter [7, 20, 21]. BYU generates HR wind images which se-

lects the ambiguity which most closely matches the nearest L2B wind, for which ambiguities selection is done by median filtering.

This thesis principally concentrates on selecting which measurements are to be used in wind retrieval and assumes that wind retrieval and ambiguity selection can be performed as they have in the past. The measurements are selected based on the amount of contamination caused by sea ice.

2.5   Ice Contamination

Retrieved winds in polar oceans are frequently contaminated by sea ice due to the radar signature of sea ice being similar to that of high wind speeds. In fact, the σ^0 distributions of wind and ice targets overlap as seen in Figure 2.6. Notice that Vpol σ^0 distribution overlap significantly for ice and ocean and that Hpol σ^0 distributions are only marginally better. This overlap makes ice contamination detection and mitigation non-trivial.
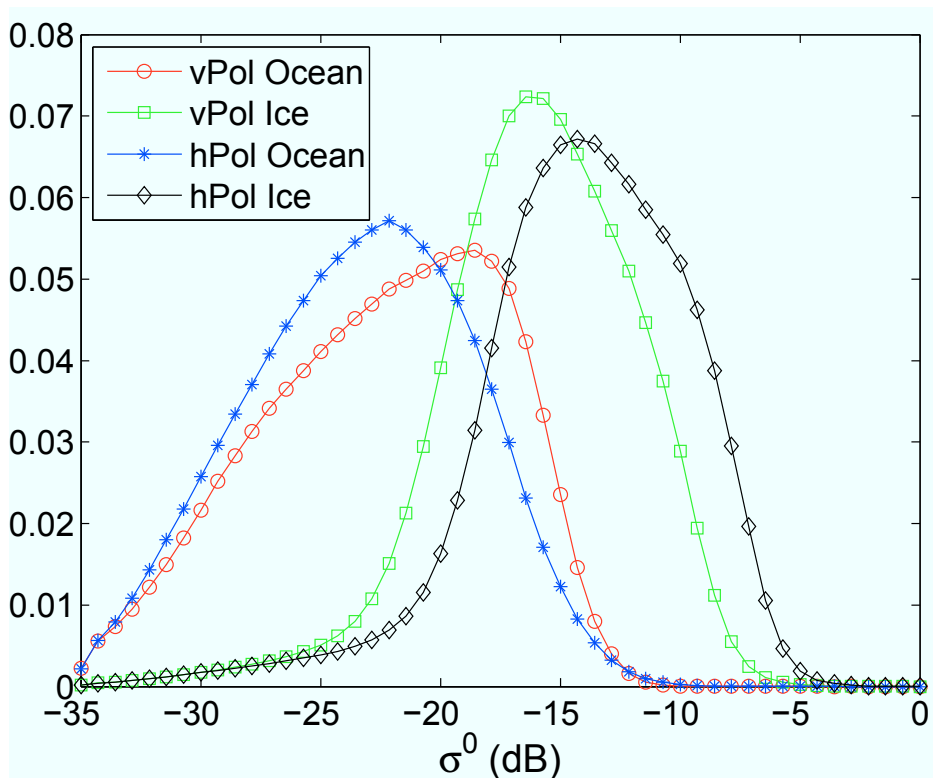
Figure 2.6: Distributions of σ^0 constructed from 2000 data in the Antarctic ocean. These plots are generated from arbitrarily sampled 2000 data of approximately 130 million WVCs.

Sea ice is constantly moving, freezing, or melting causing significant uncertainly in ice location. Sea ice has been known to drift as much as 80 km in a single day [2,3]. Furthermore, ice often breaks off of the sea-ice main extent causing more variability. Although ice detection algorithms attempt to eliminate location uncertainty, they still do not solve the problem of ice contamination in wind retrieval. This is partly due to imperfections in ice detection; however, even with perfect ice detection, the measurements next to the ice edge may be ice-contaminated.

Ice contamination can result from various amounts of ice being present within the spatial response function. Obviously a measurement is contaminated when it is completely over the ice, but it is not always trivial to detect this case. Additionally, the measurement can be contaminated if a portion of the main lobe or even side lobes contain ice. Similar land contamination has been addressed by Owen and Long [1]. The asymmetry of the spatial response function causes the measurement orientation to effect the contamination. The contamination caused by these factors is quantified by the Ice Contribution Ratio defined in the next chapter.

Ice contaminates QuikSCAT measurements in both the Antarctic and Arctic oceans. Figure 2.7 depicts the 2008 Antarctic pole, the winter and summer ice extents, and two consecutive QuikSCAT revolution swaths. Figure 2.8 shows the 2008 Arctic pole. Note that the revolutions significantly overlap, making SIR processing very advantageous in the regions. The images also demonstrate the variability in ice location throughout the year, which in turn demands a spatially dynamic contamination mitigation algorithm. Figure 2.8 shows that during the Arctic winter, most opportunity for near ice-edge wind retrieval is near Greenland, but in the Arctic summer there are regions to retrieve winds on practically all sides of the sea ice.

2.6 Summary

Scatterometers are used in remote sensing to measure the normalized radar cross-section σ^0 of the Earth's surface. When taken over the ocean, these measurements can be used to estimate wind vectors. In polar regions, sea ice can contaminate the measurements, making some wind estimates inaccurate. The remainder of this thesis presents an algorithm

14
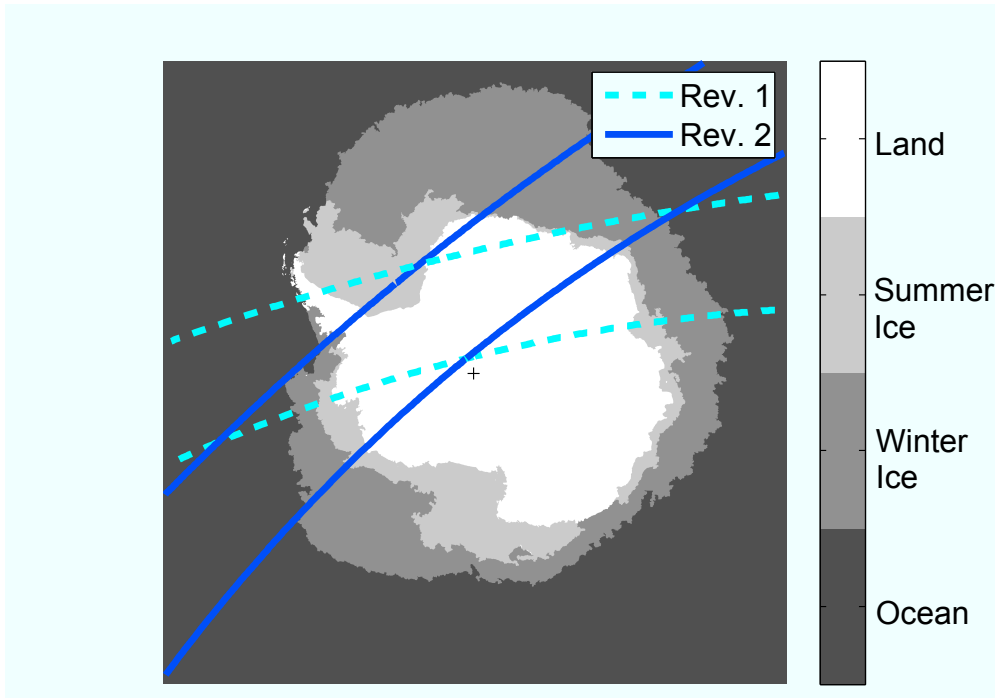
Figure 2.7: Consecutive QuikSCAT revs superimposed on an Antarctic SIR resolution image. White and black represent land and ocean. Light gray represents the sea ice extent during the 2008 summer, while the dark gray is the extent during the 2008 winter. The + indicates the south pole location.
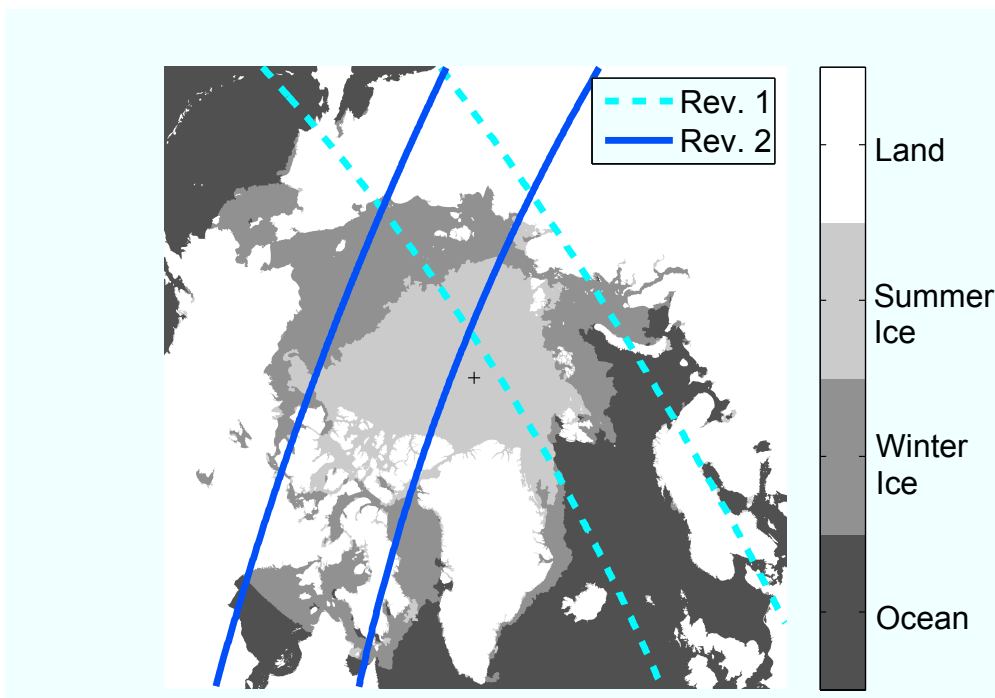
Figure 2.8: Two QuikSCAT revs superimposed on an Arctic SIR resolution image. The color bar is the same as in Figure 2.7. The + indicates the north pole location.

for detecting measurements which are contaminated be sea ice. These measurements are discarded before wind retrieval in order to maintain valid wind estimates.

Chapter 3

Ice Contribution Ratio Algorithm

This chapter presents an algorithm for mitigating sea ice contamination in QuikSCAT wind retrieval. First the ICR is developed as a σ^0 measurement model parameter. The ICR is estimated using Bayesian probability theory and used as a metric to predict the amount of ice contamination present in each measurement. The second section of this chapter describes how ICR thresholds are determined by simulation. Finally the algorithm is summarized.

3.1   ICR Model

The ICR derivation begins with the spatial response function model for σ^0_{True} as seen in Eq. (2.3), which I restate for convenience here

$$\sigma^0_{\text{True}} = \frac{\displaystyle\int_{\text{footprint}} \sigma^0(\mathbf{v})R(\mathbf{v})d\mathbf{v}}{\displaystyle\int_{\text{footprint}} R(\mathbf{v})d\mathbf{v}}. \tag{3.1}$$

Recall that this model presents each noise free measurement σ^0_{True} as a weighted average of a distributed σ^0 over the measurement footprint on the Earth's surface. The spatial response function, $R(\mathbf{v})$, is the weighting function.

The footprint area can be subdivided into two disjoint components: regions of ice and regions of ocean. The integral in the numerator of Eq. (3.1) can be subdivided into two partitions corresponding to these disjoint components. Assuming the surface backscatter of each partition separately is approximately constant over the integration area, ice and ocean

σ^0 factor out of the corresponding integrals, and Eq. (3.1) becomes

$$
\begin{aligned}
\sigma^0_{\text{True}} &= \frac{\sigma^0_i \displaystyle\int_{\text{ice}} R(\mathbf{v})d\mathbf{v}}{\displaystyle\int_{\text{footprint}} R(\mathbf{v})d\mathbf{v}} + \frac{\sigma^0_o \displaystyle\int_{\text{ocean}} R(\mathbf{v})d\mathbf{v}}{\displaystyle\int_{\text{footprint}} R(\mathbf{v})d\mathbf{v}} \\
&= \sigma^0_i \text{ICR} + \sigma^0_o \left(1 - \text{ICR}\right),
\end{aligned}
\tag{3.2}
$$

where the factored backscatter is σ^0_i for ice and σ^0_o for ocean and

$$
\text{ICR} = \frac{\displaystyle\int_{\text{ice}} R(\mathbf{v})d\mathbf{v}}{\displaystyle\int_{\text{footprint}} R(\mathbf{v})d\mathbf{v}}
\tag{3.3}
$$

is defined as the Ice Contribution Ratio.

The ICR for a given measurement is the fraction of the spatial response that is over sea ice and ranges from 0 to 1. In ICR processing, this quantity is calculated for each measurement. If the ICR is greater than a threshold, then the measurement is discarded as "ice contaminated." The ICR thresholds are generated with the aid of simulation as described in Section 3.2. First, however, a method for estimating the ICR for a given measurement is described.

3.1.1   ICR Estimation

To quantify the amount of ice contribution in each measurement, the ICR expression in Eq. (3.3) is discretized into the summations

$$
\text{ICR} \approx \frac{\displaystyle\sum_{\text{ice}} R[n]}{\displaystyle\sum_{\text{footprint}} R[n]} = \frac{\displaystyle\sum_{\text{footprint}} I[n]R[n]}{\displaystyle\sum_{\text{footprint}} R[n]},
\tag{3.4}
$$

where the indicator function $I[n]$ takes the value of 1 if location n corresponds to sea ice and 0 if it corresponds to ocean. To help account for the uncertainty in the movement of the

ice edge from day to day, $I[n]$ is treated as a binary random variable. As such, $I[n]$ has a binary probability mass function (PMF) with the probability of ocean for $I[n] = 0$ and the probability of sea ice for $I[n] = 1$. Using this PMF, an estimate for the ICR is chosen by taking the expected value of Eq. (3.4). The expected value of a binary random variable with values of 0 and 1 is simply the probability of 1 occurring, or in this case the probability of sea ice. This leads to the change from $I[n]$ to the probability $P_n(\text{ice}|\boldsymbol{\sigma}^{\mathbf{0}}_{\text{Obs}})$ of ice occurring in the nth index so that

$$\text{ICR} \approx \frac{\displaystyle\sum_{\text{footprint}} P_n(\text{ice}|\boldsymbol{\sigma}^{\mathbf{0}}_{\text{Obs}})R[n]}{\displaystyle\sum_{\text{footprint}} R[n]}. \tag{3.5}$$

This expression suggests a Bayesian approach to calculating the ICR, which is how the ICR algorithm makes this calculation. As such, $P_n(\text{ice}|\boldsymbol{\sigma}^{\mathbf{0}}_{\text{Obs}})$ is referred to as the posterior probability of ice.

The formulation in Eq. (3.5) is a new approach to quantifying the amount of spatial contribution from part of the footprint. The posterior probability makes it possible to account for the location uncertainty of the sea ice in the footprint. As the notation suggests, the probability depends on the σ^0 measurements taken at that location. However it does not depend on the measurements taken in nearby locations except for in applying the prior as discussed in the next section.

The posterior probability of ice given the observed σ^0 measurements can be calculated using Bayes' rule and the law of total probability resulting the in

$$P_n(\text{ice}|\boldsymbol{\sigma}^{\mathbf{0}}_{\text{Obs}}) = \frac{P_n(\text{ice})P_n(\boldsymbol{\sigma}^{\mathbf{0}}_{\text{Obs}}|\text{ice})}{P_n(\text{ice})P_n(\boldsymbol{\sigma}^{\mathbf{0}}_{\text{Obs}}|\text{ice}) + P_n(\text{ocean})P_n(\boldsymbol{\sigma}^{\mathbf{0}}_{\text{Obs}}|\text{ocean})}, \tag{3.6}$$

where $P_n(\text{ice})$ is the prior probability of ice and $P_n(\text{ocean}) = 1 - P_n(\text{ice})$ is the prior probability of ocean. The quantities $P_n(\boldsymbol{\sigma}^{\mathbf{0}}_{\text{Obs}}|\text{ice})$ and $P_n(\boldsymbol{\sigma}^{\mathbf{0}}_{\text{Obs}}|\text{ocean})$ are observation probabilities which are the probabilities of making the measured observations given that the nth pixel is ice or ocean respectively. Both the prior and observation probabilities are needed to calculate the posterior.

3.1.2 Prior Contribution and Generation

The first step to calculating the posterior is to generate $P_n(\text{ice})$, which is the prior probability of sea ice for the nth pixel. To construct this prior, I use the sea ice maps created by the RL algorithm, however other ice detection algorithms could also be used.

To generate the priors, daily binary RL ice maps are averaged over a time window which is non-causal including previous, current, and subsequent days. This method enables detection of ice that has disconnected from the main ice extent (disjoint ice). The results presented in this thesis are based on a time window spanning 23 days. Results for using other time windows are described in Appendix B using metrics discussed in Section 4.2.1.

It is informative to consider the construction of a prior with disjoint ice regions. During the summer melt, portions of ice may be isolated from the main ice extent and may not be mapped by the RL algorithm. Such ice typically melts within a short time, but it still causes ice contamination during the melt period. An example of this is seen in Figure 3.1, which is a HR wind estimate image contaminated by ice. The RL edge is also shown for comparison. Since undetected ice exists for only a short time, the multiple day prior results in a moderate probability of ice for the region as seen in Figure 3.2. This enables the ICR algorithm to detect areas of ice contamination even if the RL algorithm does not detect ice for that particular day.

In order to minimize the probability that disjoint ice is lost, a low but non-zero prior is assigned to locations that otherwise would be 0. Similarly a probability prior of 100% is lowered to avoid forcing ice classification.

From observation, the choice of this near-100% probability does not greatly effect the final wind results. The ICR algorithm generally rejects such regions from wind retrieval regardless of the choice of the high non-100% prior.

The choice of the non-zero low prior has little apparent effect on the boundary for which winds are retrieved. However, as the prior increases, high wind speeds in the swath center or edges appear to become more likely to be discarded from wind retrieval. High wind speeds with high priors are more likely to have high posterior probabilities because high wind speeds have similar scattering properties to that of sea ice. Wind retrieval is less accurate in the swath center and edges due to a lack of measurement azimuth diversity. Section 3.2
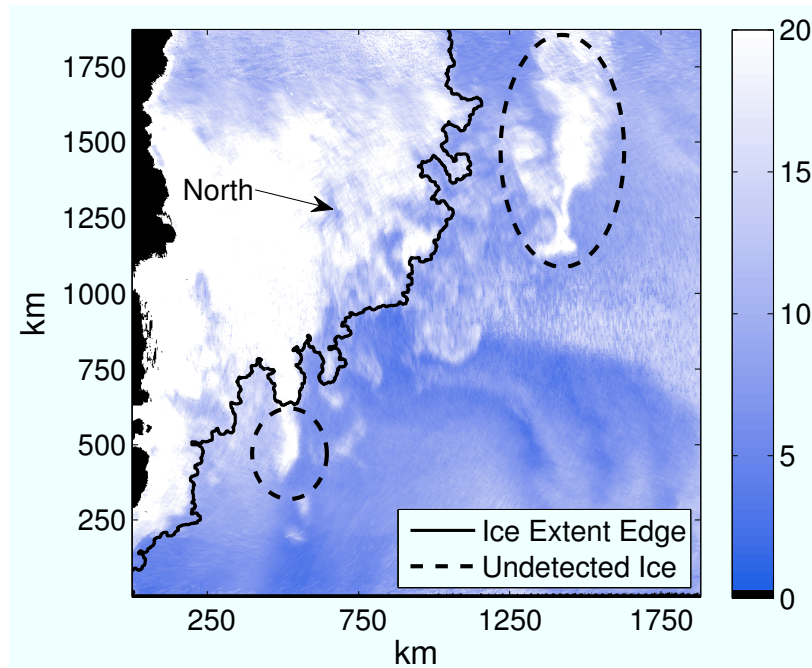
Figure 3.1: Image of wind speed estimates (m/s) for WVCs south of Africa on December 15, 2004 for orbit revolution 28590. The axes represent distances from 61.1 degrees South and 33.4 degrees East. In this image, wind speed is retrieved for all WVCs without regard to sea ice location. Ice-covered and ice-contaminated areas result in apparent high winds. The dashed lines show areas of undetected ice, disjoint from the main ice extent. The RL edge is shown as a solid line.
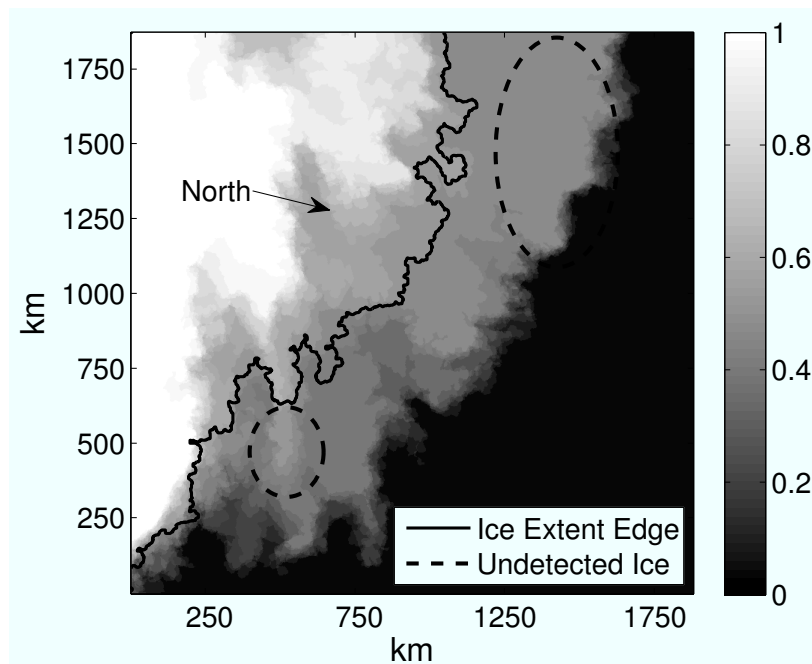
Figure 3.2: Image of prior probability of ice made by averaging 23 days of RL ice maps for the area shown in Figure 3.1.

21
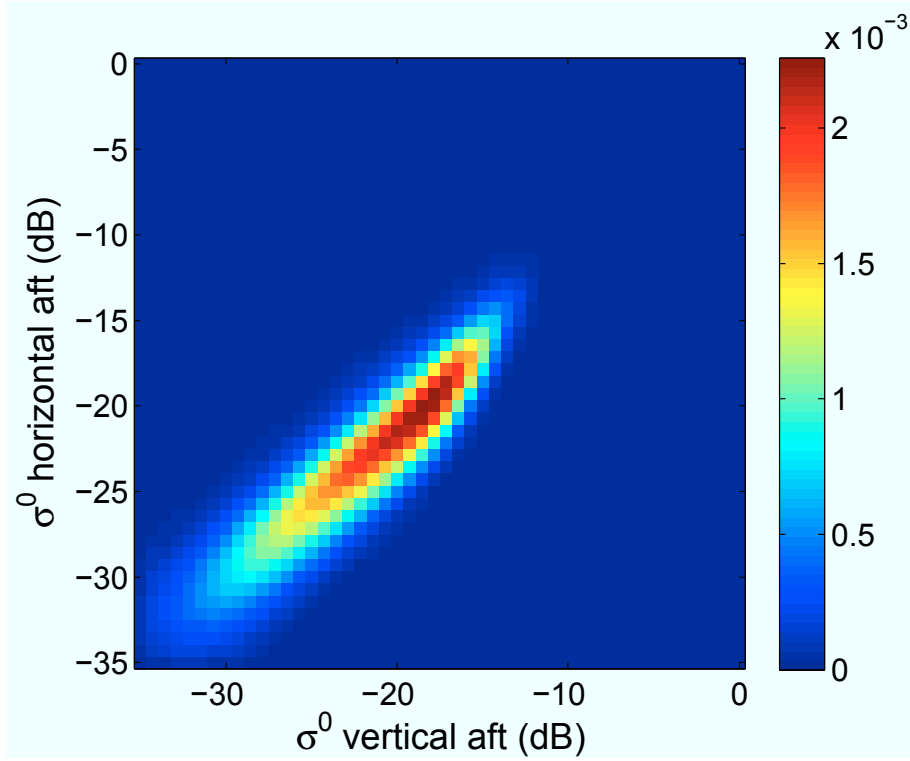
Figure 3.3: Antarctic ocean marginal observation probabilities for Hpol and Vpol aft measurements.
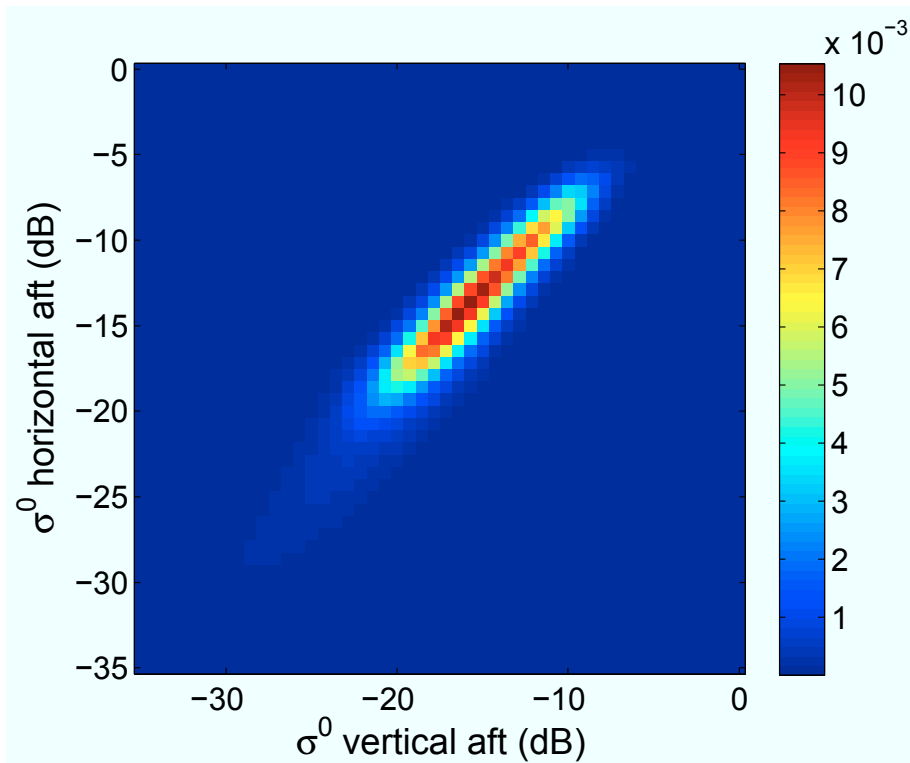
Figure 3.4: Antarctic ice marginal observation probabilities for Hpol and Vpol aft measurements.

describes how this can penalize measurements in these swath regions. The result is that a higher prior for ocean winds in the center of the swath can result in unnecessary measurement rejection. However, it is more acceptable to reject uncontaminated measurements than to accept contaminated measurements.

In this thesis, the 0% prior is raise to 4.35% which corresponds to the lowest non-zero prior that can be achieved using a 23 day prior. Similarly the 100% prior is decreased to 95.65% which corresponds to the highest non-100% prior that is achievable using a 23 day prior.

3.1.3 Observation Probability

The posterior calculation in Eq. (3.6) requires observation probabilities $P_n(\boldsymbol{\sigma}^{\mathbf{0}}_{\text{Obs}}|\text{ice})$ and $P_n(\boldsymbol{\sigma}^{\mathbf{0}}_{\text{Obs}}|\text{ocean})$. These are estimated using a year-long training set of σ^0 observations from 2004 where ice and ocean are defined by daily RL ice maps. In each region, the 4 observation types (v-pol, h-pol, fore, and aft) are binned into 4 dimensional histograms. These histograms are made on a monthly basis and are normalized to obtain the observation probability estimates.

Figure 3.3 and Figure 3.4 show ocean and ice marginal observation probabilities for 2004 as functions of Vpol and Hpol aft σ^0 measurements. Features of these distributions are that ice generally has higher σ^0 than ocean and that the ocean distribution has a higher variance than ice. Notice there is some overlap in the distribution domains.

Finally, the posterior is calculated using the prior and observation probabilities according to Eq. (3.6), where the measured σ^0_{Obs} is taken from the AVE processed σ^0 field. The posterior assigns high probabilities over regions of disjoint ice as seen in Figure 3.5. With this posterior in place, the ICR can be calculated for each measurement.

The ICR algorithm eliminates measurements that have an ICR above a location-specific threshold to ensure that measurements are not ice contaminated. These ICR thresholds are determined through simulation as described in the next section.
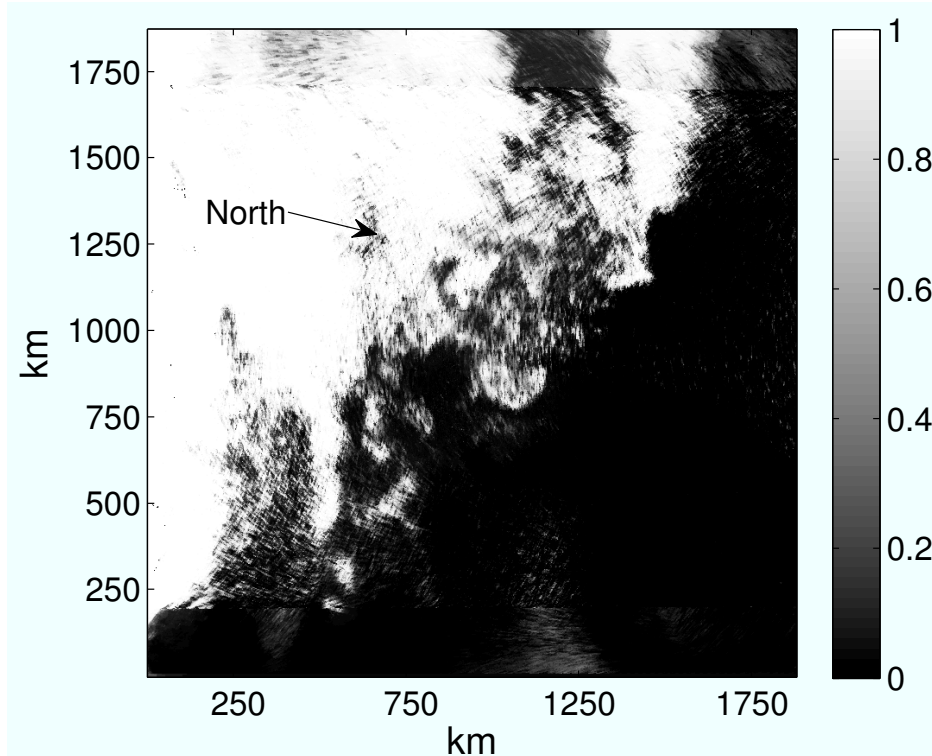
Figure 3.5: Image of the values of the posterior probability of sea ice for each pixel in the area shown in Figure 3.1.

3.2 Threshold Determination

ICR processing discards a σ^0 measurement if its ICR is greater than an allowable ICR threshold in order to bound the estimated wind speed error. Unfortunately, wind error cannot be expressed analytically due to the complexities of the GMF. However, the wind error can be analyzed using Monte-carlo simulations which enables an evaluation of how the wind error is affected by different values of ICR, wind speed, direction, σ_i^0, and cross track. The objective of the simulations is to determine which values of ICR result in excessive RMS wind speed error for given wind, σ_i^0, and cross track location. In the ICR algorithm, we use the wind direction that causes the highest error in order to be conservative [1].

The simulation uses the noisy measurement ICR model obtained by combining Eq. (2.2) and Eq. (3.2):

$$\sigma_{\text{Obs}}^o = \left(\sigma_i^0 \text{ICR} + \sigma_o^0\left(1 - \text{ICR}\right)\right)\left(1 + K_p\eta\right). \tag{3.7}$$

24

The wind GMF provides a mapping between the winds and σ_o^0. For the simulation, I choose discrete values of σ_i^0 ranging from 0.0125 to 0.5, ICR values from 0 to 0.8192, and wind speeds from 3 to 30 m/s. These ranges are chosen to exhaust the nominal values of the parameters.

The final simulation parameter is the cross-track swath location. The cross-track dependence takes into account the scatterometer's wind retrieval performance which varies across the swath.

The simulation is performed for each combination of simulation parameters. First it creates a wind field with uniform wind speed and direction from the simulation parameters. This wind field is projected through the GMF to obtain the σ_o^0 values for the slice measurements. The ocean backscatter σ_o^0 combines with the ICR and σ_i^0 parameters in Eq. (3.7) to simulate ice contamination, after which Monte-carlo noise is added to obtain σ_{Obs}^0 for each slice.

The next step is to process simulated observations with the AVE algorithm, followed by wind retrieval to obtain winds. For each set of parameters (ICR, σ_i^0, wind speed, and cross-track location), I simulate 1500 HR WVCs [1]. The retrieved wind for each WVC is compared to the original true wind to calculate RMS wind speed error.

Figure 3.6 shows the simulated RMS wind speed error as function of ICR and wind speed. These particular results occur for $\sigma_i^0 = 0.0375$ at the 7th cross track bin. Note that the RMS error increases with wind speed for the ice free case (an ICR of -40dB) This results in part from the multiplicative noise associated with scatterometer measurements as seen in Eq. (3.7). Also notice that while the RMS error increases as more ice is present (a higher ICR), there is a drop in error between 10 and 20 m/s. This "trough" in error shifts and scales in wind speed depending on σ_i^0 and cross track location demonstrating the importance of making the simulations dependent on wind speed, σ_i^0, and cross track.

To select thresholds, a relative RMS error metric is defined as

$$\epsilon_{\text{rel}} = \frac{\epsilon_{\text{Ice}} - \epsilon_{\text{Ice Free}}}{\epsilon_{\text{Ice Free}}}, \tag{3.8}$$
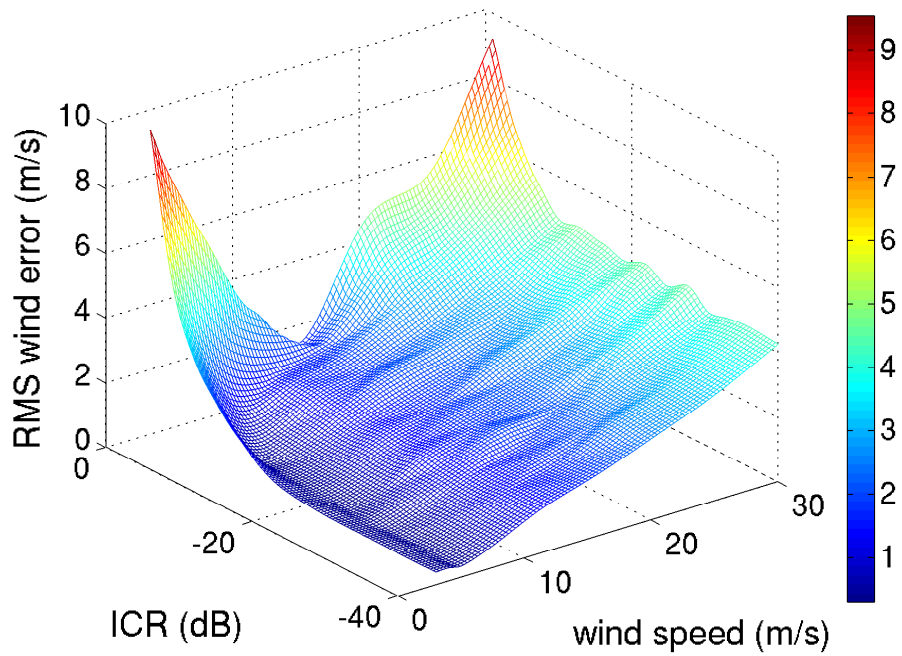
Figure 3.6: Simulated RMS wind speed error in m/s as function of ICR in dB and wind speed in m/s. These RMS wind errors are for a 0.0375 σ_i^0 and the 7th cross track bin.
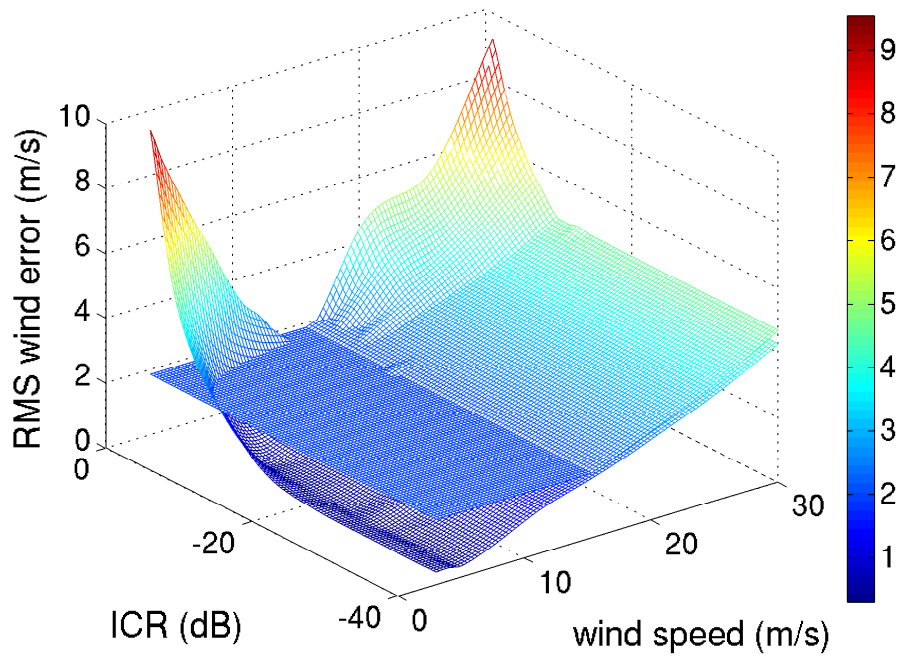

Figure 3.7: Simulated RMS wind speed error and error thresholds as functions of ICR and wind speed for the same case as shown in Figure 3.6.

where ϵ_{Ice} is the RMS wind speed error for ice contaminated winds and $\epsilon_{\text{Ice Free}}$ is the RMS wind speed error for ice free (uncontaminated) winds. The error $\epsilon_{\text{Ice Free}}$ is obtained through simulation with the same wind and cross track parameter as ϵ_{Ice} but with ICR $= 0$.

The RMS error thresholds are selected by defining a ϵ_{rel} threshold for high wind speeds and a constant RMS error threshold for low wind speeds. Figure 3.7 demonstrates the thresholding process by superimposing the RMS error thresholds on top of the simulated RMS error of Figure 3.6. For high wind speeds, I arbitrarily choose to threshold ϵ_{rel} at 10%. This results is a wind speed dependent RMS error threshold that is the diagonal plane at high wind speeds in Figure 3.7.

If the ϵ_{rel} threshold results in an RMS error less than 2 m/s then the threshold is set to 2 m/s RMS error as seen in the horizontal plane at low wind speeds in Figure 3.7. This is chosen to comply with QuikSCAT mission objectives which require RMS wind speed error to be below 2 m/s for low wind speeds [22]. The RMS error thresholds correspond to the maximum tolerable RMS wind speed error due to ice contamination for each set of σ_i^0, wind speed, and cross-track location. The corresponding maximum ICR which results in less than the RMS wind error threshold is termed the ICR threshold. These ICR thresholds are the points where the horizontal and diagonal plains cross the simulated RMS errors in Figure 3.7.

Thus the simulations determine an ICR threshold for each σ_i^0, wind speed, and cross-track location. To illustrate typical ICR thresholds, Figure 3.8 shows the thresholds averaged over all cross-track locations. Low ICR thresholds mean that even small portions of ice in a measurement significantly impact the winds, while large ICR thresholds suggest the wind retrieval is less sensitive to ice. For example, low ICR thresholds are associated with low wind speeds and high σ_i^0. This is intuitive because ice with high σ_i^0 in a low wind (low σ_o^0) environment biases the overall σ_{Obs}^o upward away from σ_o^0. Inversely, high wind speeds and higher σ_i^0 are associated with high ICR thresholds meaning that they are less sensitive to the ice. In this case the σ_i^0 and σ_o^0 are comparable, so that σ_{Obs}^o is only minimally affected by the ice contamination. Note that the threshold actually decreases at the highest wind speeds and lowest σ_i^0. This is a manifestation that simulation predict that hurricane winds
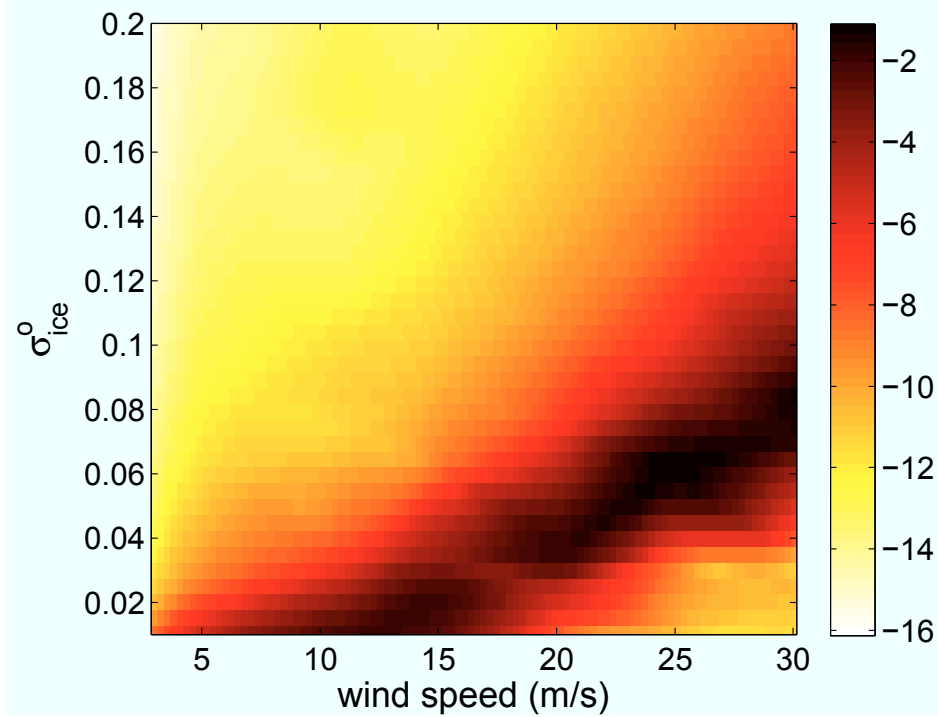
Figure 3.8: Plot of the ICR threshold in dB as a function of wind speed and ice backscatter. The value shown is the average taken across all the cross-track locations.

could be biased downward if σ_i^0 were small enough. This case is not explored in detail here because its occurrence is very unlikely.

3.3 ICR Algorithm Summary

A summary of the ICR algorithm is given in the following steps:

1. Precompute ICR thresholds by simulation.

2. Precompute observation probability distributions from a training set.

3. Compute prior probability of ice using RL ice maps in a temporal window.

4. For each revolution, use the AVE algorithm to create WVCs in the region of interest with the 4 azimuth types.

5. Calculate the posterior probability of ice using products of step 2) through 4) and Eq. (3.6).

6. Calculate the ICR for each slice measurement in the region of interest using Eq. (3.5).

7. Discard slice measurements with ICR above the ICR thresholds computed in step 1).

8. Using remaining σ^0 measurements, apply the AVE algorithm and wind retrieval to make HR or conventional wind fields.

This results in winds whose RMS error due to ice contamination are assured to be less than the error thresholds. Note that every ICR wind product employs the same thresholds and observation probabilities enabling them to be computed in preprocessing. The remainder of the steps can be executed in real time.

Chapter 4

ICR Algorithm Validation

This chapter validates and analyzes the performance of the ICR algorithm. The algorithm's success is first demonstrated via case studies. Second, in order to validate large data sets, performance metrics are measured for ICR and L2B retrieved winds. Finally, wind speed distributions are used to further validate the improved performance of large data sets of ICR winds compared to L2B winds.

4.1 Case Studies

Three case studies are considered here to demonstrate that ICR processing mitigates ice contamination and retrieves more WVCs than the L2B product. Case study 1 is from orbit revolution 28590 during the 2004 Antarctic melting period on December 15 south of Africa. Case study 2 is from orbit revolution 6367 in the 2000 Antarctic winter on October 8 east of the Drake Passage. Case study 3 is from orbit revolution 3892 in the 2000 Arctic Ocean around the Savlbard island group on March 18, 2000. The choice of these case studies is such as to give the reader intuition about how ICR processing effects wind retrieval in comparision to the L2B product.

Case study 1 demonstrates the ice contamination mitigation capability of the ICR processing. The case study is selected to demonstrate the utility of the ICR in the melting period. This day is specifically chosen because it contains large amounts of disjoint ice that are easily distinguished by the reader. As shown in Figure 4.1, L2B winds are highly contaminated, while HR ICR processed winds in Figure 4.2 exclude ice contaminated regions. Agreeing with the HR product, the conventional 25 km ICR product as shown in Figure 4.3 is contamination free. ICR processing effectively removes 573 contaminated conventional WVCs from the L2B product, while also adding 100 WVCs not retrieved by the L2B product.

Figure 4.1: Image of conventional L2B wind speeds (m/s) produced by discarding all measurements within 50 km from the RL sea ice edge (shown in gray) for the region shown in Figure 3.1. Wind is not retrieved in black regions.

Figure 4.2: Image of high-resolution wind speeds (m/s) produced using ICR processing for the area shown in Figure 3.1. Wind is not retrieved in black regions. The RL ice edge is shown for comparison.
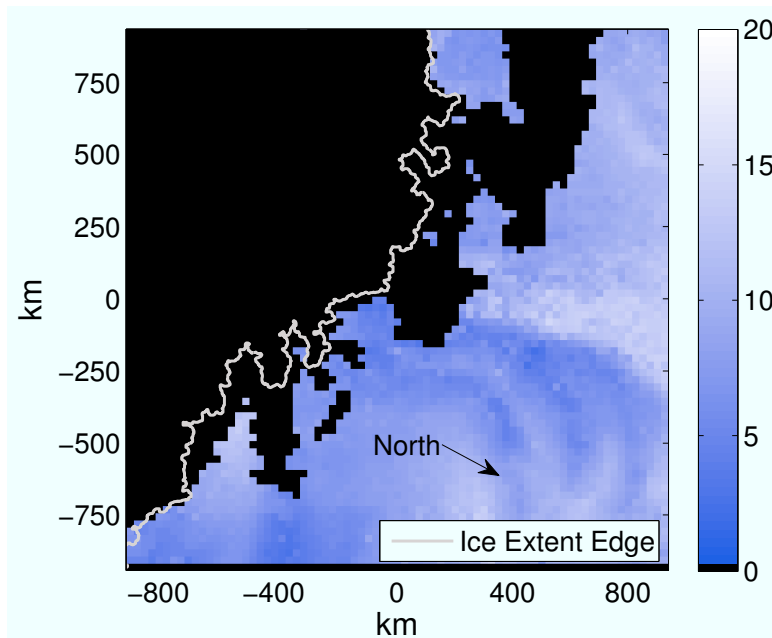
Figure 4.3: Image of conventional wind speeds (m/s) produced using ICR processing for the area shown in Figure 3.1. Wind is not retrieved in black regions. The RL ice edge is shown for comparison.
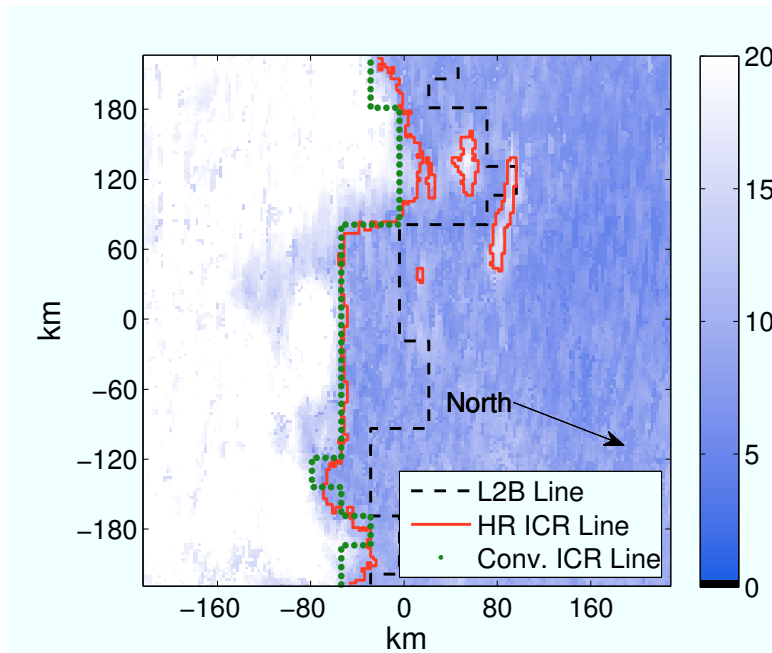
Figure 4.4: Image of high-resolution wind speeds (m/s) retrieved without regard to ice conditions east of the Drake Passage with lines representing the boundary of retrievable winds using L2B product and the ICR processed product. The data is taken from October 8, 2000 for orbit revolution 6367. The axes represent distances from 58.0 degrees South and 40.3 degrees West.
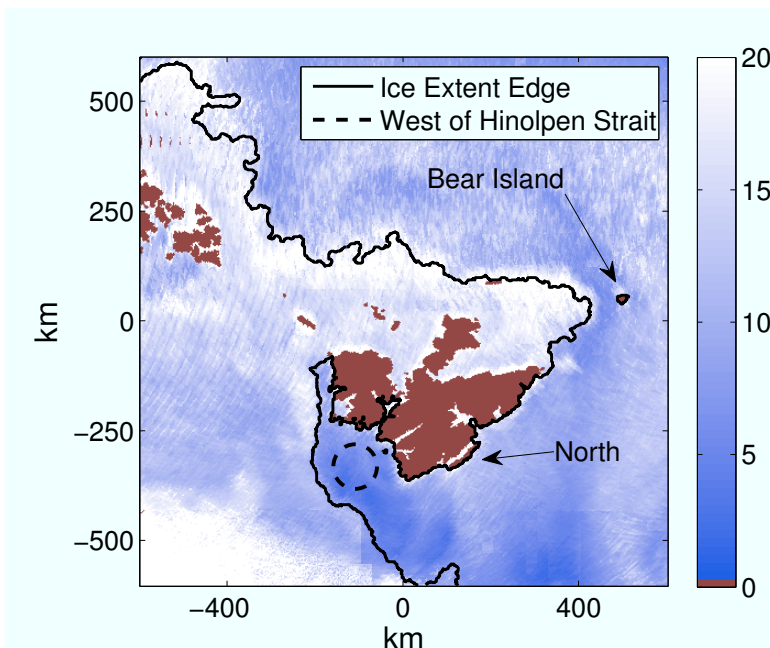
Figure 4.5: Image of wind speed estimates (m/s) for WVCs around the Svalbard island group in the Arctic ocean on March 18, 2000 for orbit revolution 3892. The axes represent distances from 78.5 degrees North and 26.5 degrees East. In this image, wind speed is retrieved for all WVCs without regard to sea ice location. Ice-covered and ice-contaminated areas result in apparent high winds. Areas of land such as Svalbard are indicated by maroon. A region west of the Hinolpen Strait is shown by a dashed circle, and the RL edge is shown as a solid line. Additionally, Bear island is indicated.
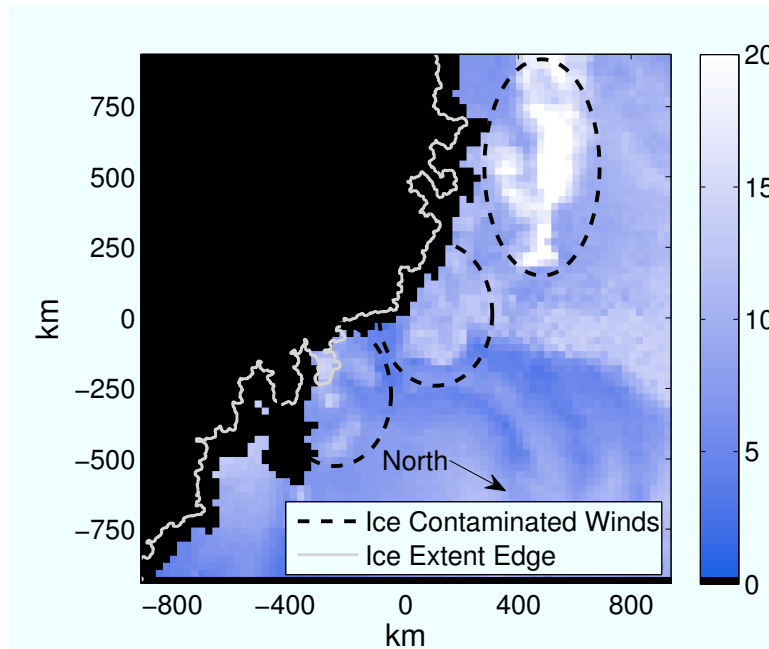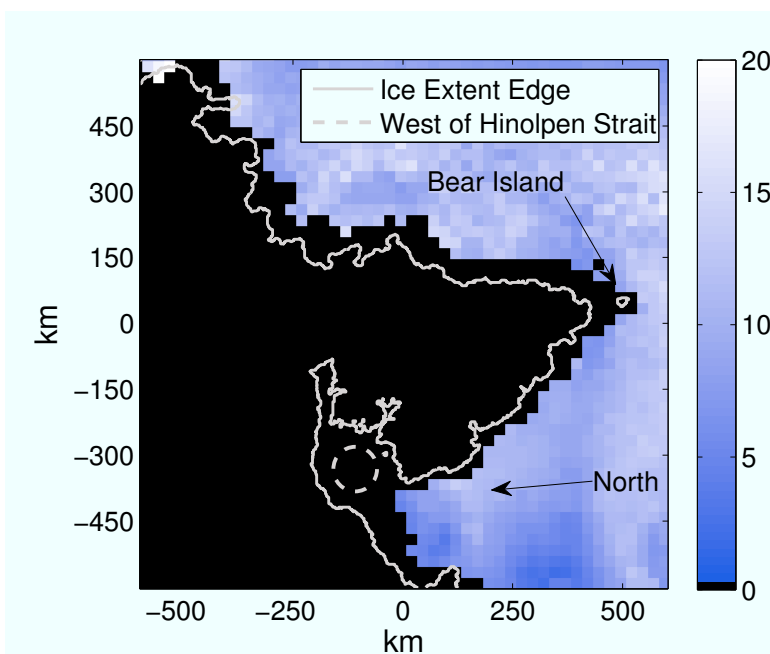

Figure 4.6: Image of conventional L2B wind speeds (m/s) produced by discarding all measurements within 50 km from the RL sea ice edge (shown in gray). The region is the same as shown in Figure 4.5. Wind is not retrieved in black regions.
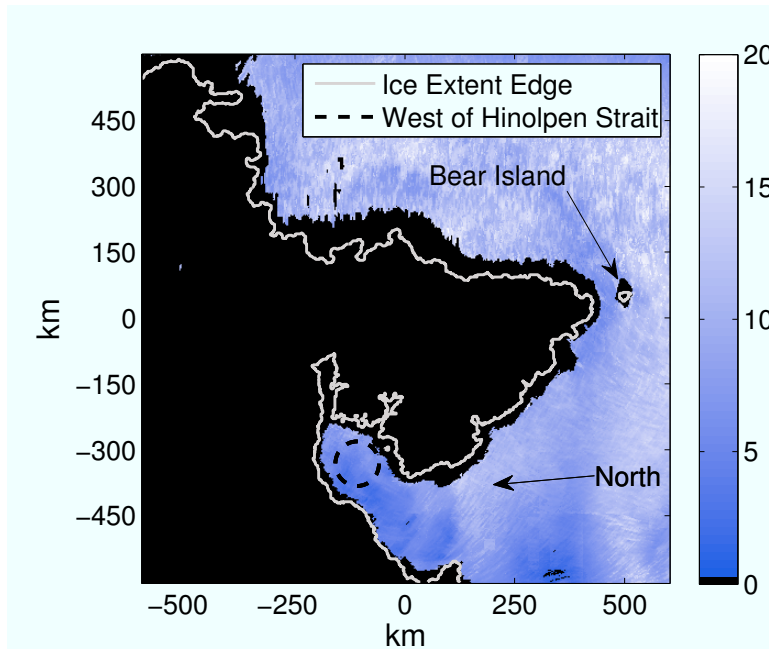
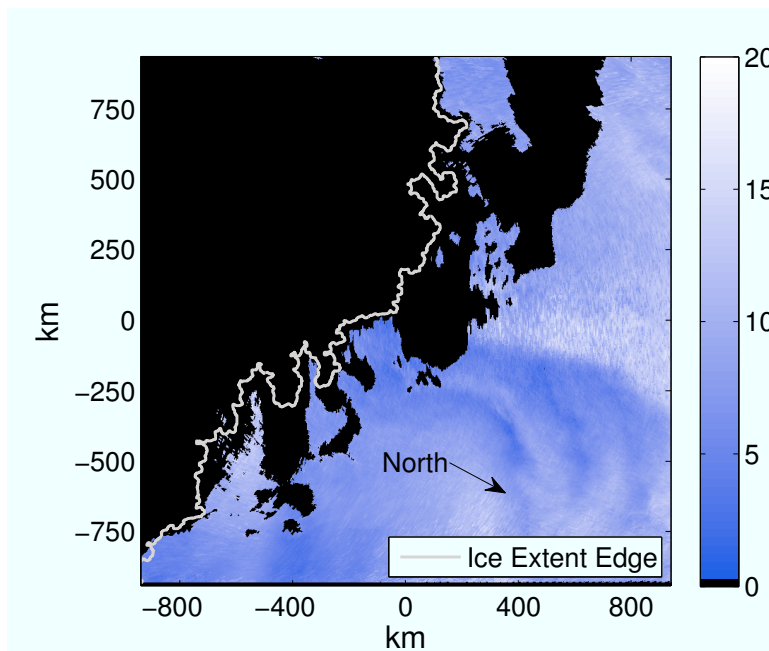**Figure 4.7:** Image of high-resolution wind speeds (m/s) produced using ICR processing for the area shown in Figure 4.5. Wind is not retrieved in black regions. The RL ice edge is shown for comparison.
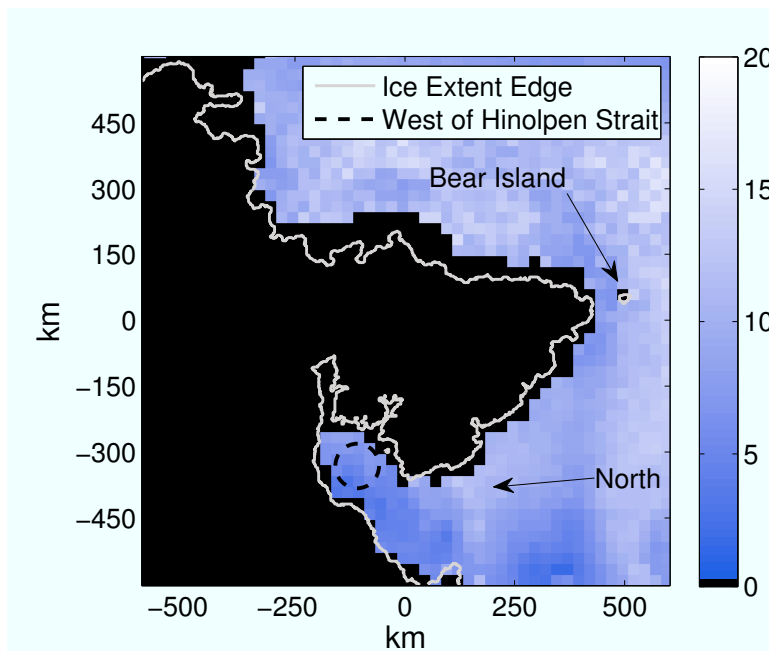
Figure 4.8: Image of conventional wind speeds (m/s) produced using ICR processing for the area shown in Figure 4.5. Wind is not retrieved in black regions. The RL ice edge is shown for comparison.

ICR processing typically retrieves more uncontaminated WVCs than the L2B product. Case study 2 is arbitrarily selected to demonstrate this typical outcome of the algorithm. Figure 4.4 shows wind speeds retrieved for all WVCs without regard to sea ice location. To illustrate winds retrieved by different methods, the 3 superimposed lines represent the boundary of retrieved winds in the L2B, HR ICR, and conventional ICR products. To the left of these lines are ice-contaminated winds, while to the right are uncontaminated winds. The ICR lines are much closer to the sea ice than the L2B line, resulting in 59 more conventional WVCs in this small region. Furthermore, 308 more conventional WVCs are retrieved over the entire swath exemplifying that ICR processing can retrieve winds closer to ice than the conventional 50 km distance.

Case study 3 is chosen to demonstrates that the algorithm can retrieve winds closer to sea ice than the L2B and that the algorithm can operate in the Arctic ocean. Figure 4.5 is an image of wind speeds estimated without regard to sea ice location near the Svalbard island group. Figure 4.6 is the L2B product for the same region. Notice that the large region west of the Hinolpen Strait (shown with a dashed circle) is excluded from wind retrieval. The small ocean area between Bear island and the ice edge is also excluded. However, in the Figure 4.7 HR ICR product, winds are retrieved in both of these locations increasing coverage. This is also seen in the conventional resolution ICR product seen in Figure 4.8. A total of 100 more conventional WVCs are retrieved in this image compared to the L2B product while also excluding 26 contaminated WVCs from the L2B product.

These case studies demonstrate that the ICR algorithm both excludes ice contamination and increases the number of uncontaminated WVCs. The large set validation that follows further demonstrates these points.

4.2   Large Set Validation

This section presents performance analysis for the ICR algorithm for several large time series in the northern and southern hemispheres for 2000, 2004, and 2008. For this study the observation probabilities $P_n(\boldsymbol{\sigma}^{\mathbf{0}}_{\mathrm{Obs}}|\mathrm{ice})$ and $P_n(\boldsymbol{\sigma}^{\mathbf{0}}_{\mathrm{Obs}}|\mathrm{ocean})$ are estimated using the 2004 Antarctic as a training set, while the 2000 and 2008 time series are the withheld sets.

The success in the Arctic, using an Antartic training set, demonstrates that the algorithm is robust in its training set dependence.

The time series contain a variable number of revolutions. The 2000 and 2004 Antarctic time series have a combined 553 revolutions sampled arbitrarily throughout the year. The Arctic 2000 and 2004 time series have a combined 333 revolutions selected arbitrarily within regions and times for which the metrics can be easily measured. The 2008 time series contains the much larger sampling of 5133 revolutions for the Antarctic and 3593 for the Arctic. Validation is performed on all these time series.

To aid in analysis, the following two metrics are defined to measure ice proximity and wind speed error. The wind speed error metric requires local uncontaminated winds which are discussed. The metrics are used to measure the algorithm's success in the 2000 and 2004 time series. Finally, wind distributions are compared as a validation for the 2008 time series.

4.2.1 Validation Metrics

Two metrics measure the ICR algorithm's success. The first is the standoff distance (SOD), and the second is relative RMS wind speed error.

The SOD measures the distance from the sea ice edge that wind can be retrieved by a given algorithm. To calculate this, the ICR-determined WVCs which are closest to the ice edge are identified. Then the SOD is defined as

$$\text{SOD} = \text{mean}(d_1, d_2, ...d_N), \tag{4.1}$$

where d_i is the shortest distance to a ice pixel edge center from the center of the ith WVC as illustrated in Figure 4.9.

The relative RMS wind speed error ϵ_{rel} is the same metric as defined in Eq. (3.8), except that in this case ϵ_{Ice} is the RMS error of ICR-determined winds near the ice edge while $\epsilon_{\text{Ice Free}}$ is still the RMS wind speed error for ice free (uncontaminated) winds. To calculate error, I use a wind product from the National Centers for Environmental Prediction (NCEP) for comparison [23].
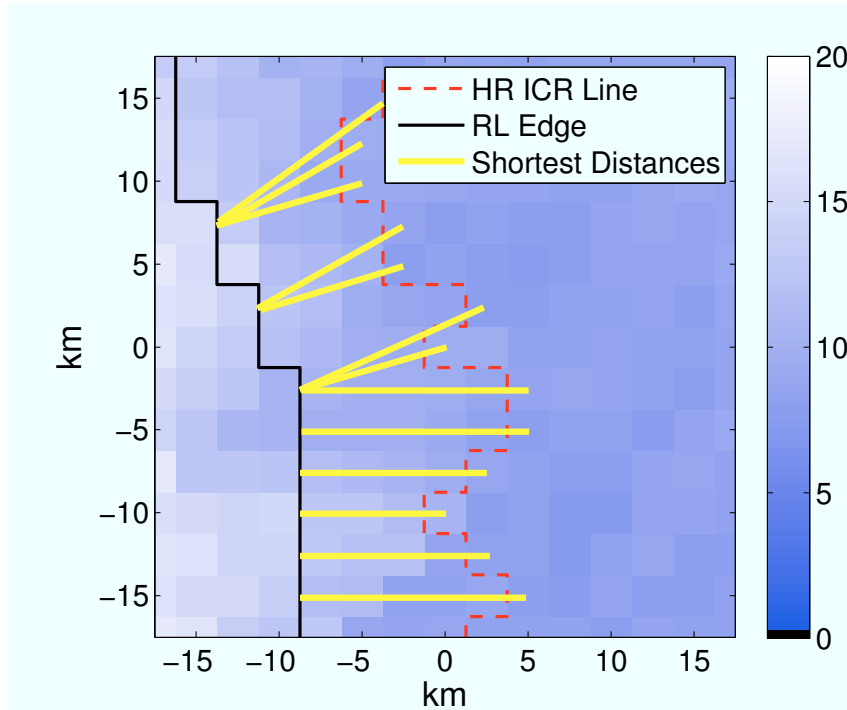
Figure 4.9: Illustration of the ice edge and the HR ICR line superimposed on a wind speed field (m/s). The wind speeds in this image are retrieved for all WVCs without regard to sea ice location. The yellow lines are the shortest distance from the center of each WVC along the HR ICR line to a ice pixel edge center. The SOD is defined as the mean of these distances.
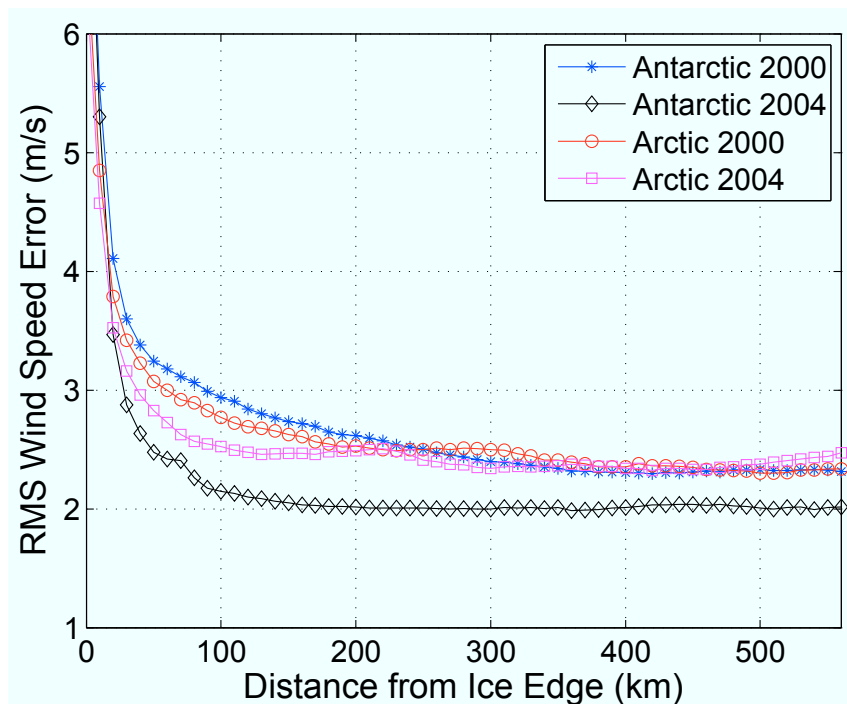
Figure 4.10: RMS wind speed error as a function of distance from the RL ice edge for the winter and summer 2004 time series using NCEP for comparison. Sets contain more than 8 million WVCs

38

4.2.2 Local Ice Free Winds

To approximate $\epsilon_{\text{Ice Free}}$, I investigate winds found a short distance away from the ICR-determined winds. In execution, I take care that $\epsilon_{\text{Ice Free}}$ winds are sufficiently far from sea ice to guarantee no ice contamination. Over the short distances, wind statistics are assumed to be approximately constant as will be investigated. This is important because I want any major differences between ϵ_{Ice} and $\epsilon_{\text{Ice Free}}$ to be only due to ice contamination.

In order to evaluate how constant the RMS wind error is over short distances, I measure the RMS wind speed error as a function of distance from the RL ice edge. In using the RL edge, one must be careful to exclude free floating ice in the analysis since the RL maps only show ice connected to the main body. Figure 4.10 shows RMS speed errors as a function of distance from the ice edge for the four time series. The initial drop in RMS error is due to the drop in ice contamination as one moves away from the edge. After this, the error reaches a floor related to normal wind retrieval skill, which validates our assumption of locally constant wind statistics. The changes in error when further than 100 km are comparatively small and are attributed to changing wind statistics. Based on these results, I cautiously average the RMS error between 100 and 200 km to use as $\epsilon_{\text{Ice Free}}$ in Eq. (3.8).

4.2.3 ICR Metric Performance Results

The ϵ_{rel} and SOD are measured for the four time series from the HR ICR winds, conventional ICR winds, and L2B winds as shown in Table 4.1. These results are achieved using a 23 day prior and are generated from 886 orbit revolutions. For the L2B case, 3 revolutions that otherwise would be used are excluded because of severe and obvious contaminated wind retrieval performed over ice shelves. This enables a fairer comparison between the L2B and ICR products. Conventional ICR and L2B products combine more than 100,000 WVCs to measure each metric. HR ICR SOD uses approximately 0.5 million WVCs, while ϵ_{rel} uses approximately 1 million WVCs.

The ICR SOD is consistently lower than the L2B SOD in all four time series indicating that ICR processing retrieves winds closer to the ice edge than the L2B product. In the Antarctic ocean, HR and conventional ICR winds are retrieved on average 38.4 km closer,

Table 4.1:
SOD and relative RMS error ϵ_{rel} results for ICR processed winds next to the ice edge. These results are achieved using a 23 day prior.

Metric	Set	HR	Conventional	L2B
SOD (km)	Antarctic 2000	22.7	22.8	57.9
	Antarctic 2004	22.9	23.1	64.7
	Arctic 2000	22.1	22.2	38.7
	Arctic 2004	22.0	21.8	37.2
ϵ_{rel} (%)	Antarctic 2000	21.7	18.1	31.6
	Antarctic 2004	30.4	27.3	34.3
	Arctic 2000	16.5	20.6	31.2
	Arctic 2004	21.9	26.7	40.0

while they are 15.9 km closer in the Arctic ocean. Thus the greatest increase in SOD performance is seen in the Antarctic ocean.

With an average SOD of 22.5 km, HR and Conventional ICR winds have remarkably little SOD deviation. The consistency of the SOD measurements between years demonstrates the algorithm's consistency between the 2000 withheld set and 2004 training set.

The ϵ_{rel} metric is lower for ICR products than for the L2B product, demonstrating that the WVCs near the ice edge have less ice contamination in ICR winds than in the L2B winds. Unfortunately, ϵ_{rel} exceeds the 10% target set in Section 3.2 by a factor of 2 to 3 and has more variability than the SOD. In part, this can be attributed to upsampling and error of the NCEP winds used for comparison. Another possible origin is that the target relative error is actually larger than 10% for low wind speeds as described in Section 3.2. Still, ICR products improve upon the L2B product with lower ϵ_{rel} in all cases. In order to further demonstrate the algorithm's effectiveness, wind distributions are analyzed.

4.2.4 Wind Distributions

The probability distributions of wind can be used to validate the removal of ice contamination because wind statistics are approximately constant over short distances in the open ocean. Thus, wind statistics should be about the same near the ice edge as they

are a short distance from the edge. If ice contamination is present, wind speeds will be higher than they otherwise would be.

Wind distributions are used to demonstrate the effectiveness of ICR processing in 2008 for Antarctic and Arctic winds. Figure 4.11 shows wind speed distributions for the Antarctic ocean and Figure 4.12 for the Arctic ocean, where each figure contains distributions consisting of the following:

1. Conventional WVCs retrieved using ICR processing, for which the L2B product also retrieves winds.

2. Conventional WVCs retrieved in L2B product, for which ICR processing also retrieves winds.

3. Conventional WVCs retrieved using ICR processing, for which the L2B product does not retrieve winds.

4. Conventional WVCs retrieved in L2B product, for which ICR processing does not retrieve winds.

Distributions 1) and 2) are from WVCs for which both the L2B and ICR processed products agree on performing wind retrieval within 100 km. Although the WVC locations are the same for these distributions, different slices may be used for wind retrieval. Note that sets 1) and 2) agree well in Figure 4.11 and also separately agree in Figure 4.12. These distributions are likely ice free since they are constructed using data which both ICR and L2B agree is uncontaminated. They require that both the ICR and L2B products agree. Because they are so similar, they are a good target for both ICR and L2B winds to test for ice contamination.

Distribution 3) closely matches 1) and 2) in both figures. This demonstrates that ICR processing results in WVCs that are uncontaminated by ice.

Demonstrating contamination, distribution 4) has a mode that occurs at a much higher wind speed than the uncontaminated distributions as well as a high tail in the highest wind speeds. This is expected for ice contaminated winds because ice has a similar radar signature to that of ocean at high wind speeds. One would not expect such a drastic change in wind statistics given that the WVCs are taken from an area approximately the same as

41
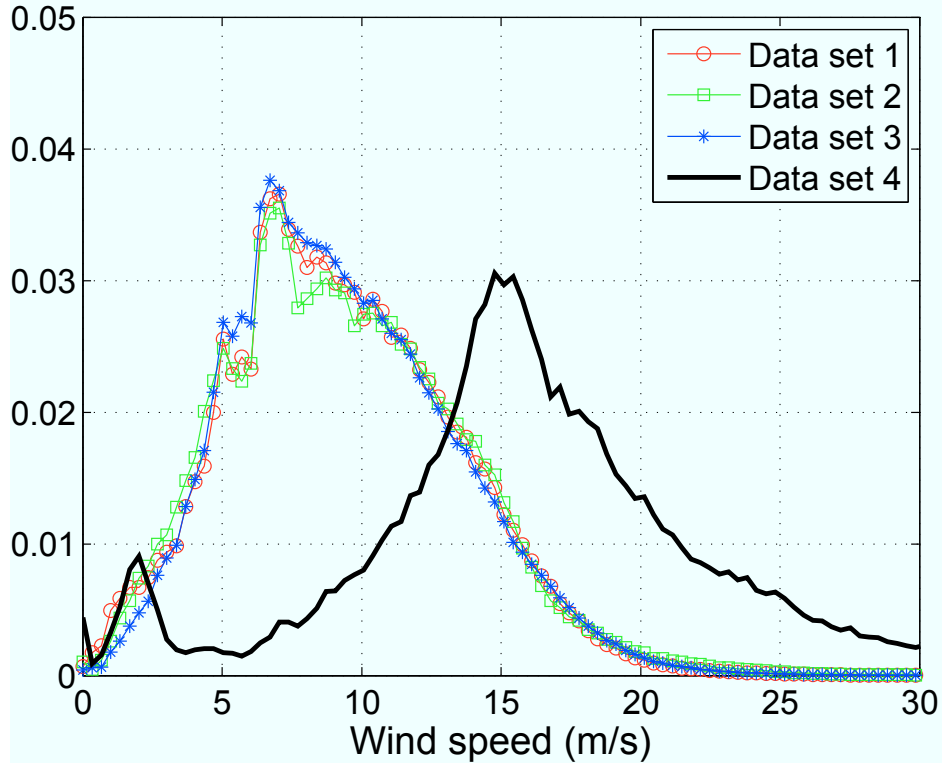
Figure 4.11: Wind speed distributions in the Antarctic ocean taken from 5,133 QuikSCAT ascending passes during 2008. Winds in the ice edge region are broken into four different sets: 1) WVCs retrieved using ICR processing which are also retrieved by the L2B product; 2) WVCs retrieved by L2B product which are also retrieved using ICR processing; 3) WVCs retrieved by ICR processing but considered ice contaminated by the L2B product; and 4) WVCs retrieved by the L2B product but considered ice contaminated by ICR processing. There are more than 4 million WVCs in the combined data sets.

the other distributions. This leads to the conclusion that the L2B product's distribution is contaminated by ice which ICR processing is capable of mitigating.

4.3 Summary

Case study investigation indicates the success of ICR processed winds in both retrieving more WVCs and resulting in less ice contamination than the L2B product. These results are also seen in performance analysis using the two metrics defined previously. Furthermore, wind distributions suggest that ICR processing mitigates ice contamination compared to the L2B product.
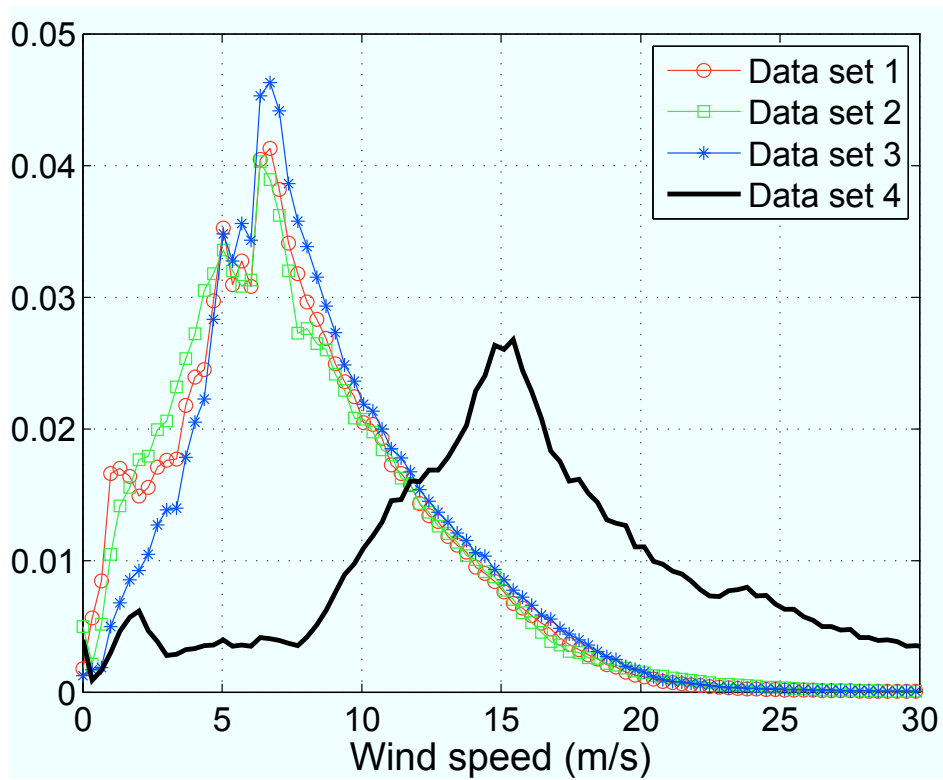
Figure 4.12: Wind speed distributions in the Arctic ocean taken from 3,593 QuikSCAT descending passes during 2008. The explanations for the four distribution data sets is described in Figure 4.11. There are more than 6 million WVCs in the combined data sets.

Chapter 5

Conclusion

In conclusion, by using the Ice Contribution Ratio, wind retrieval can be performed approximately 22.5 km from the sea ice edge while sustaining wind retrieval integrity. This is a huge distance improvement over the JPL standard algorithm which merely dilates the ice edge by 50 km before retrieving winds. Furthermore, ICR processing results in less RMS wind speed error than the JPL algorithm applied on the current L2B product. ICR processing can be applied to HR or conventional WVCs for either Arctic or Antarctic oceans in any year of QuikSCAT's mission. The principle components and results of this thesis have been submitted for publication.

The following section summarizes this thesis' contribution to the remote sensing community. The succeeding section addresses future possible research avenues.

5.1 Thesis Contributions

This thesis develops an algorithm for mitigating sea ice contamination in QuikSCAT wind retrieval. To mitigate contamination, each slice measurement is investigated by measuring the Ice Contribution Ratio, which describes the spatial support of ice in the measurement footprint. The ICR accounts for the uncertainty of the ice location using Bayesian probability theory which utilizes prior and observed distributions to calculate a posterior. The posterior, combined with the spatial response function, enable the ICR calculation for each measurement. Slice measurements are discarded from wind retrieval if their ICRs exceed a threshold, which depends on swath location, wind conditions, and ice σ^0. ICRs thresholds are determined via simulation using a model which relates ICR to a measured σ^0.

In addition to mitigating contamination, the algorithm enables more WVC's to be retrieved than previously possible. Accurate winds can now be retrieved as close as 22.5

km away from the ice edge. ICR processing is operational in both the Antarctic and Arctic oceans. In addition to and as elements of the ICR algorithm, the following contributions are also listed in subsequent sections.

5.1.1 Ice Contribution Metric

An ice contamination metric, the ICR, is derived to be used for ice contamination mitigation. This metric measures how much of the spatial response function is over sea ice, and is calculated using a Bayesian approach which models the uncertainty in ice location. Additionally, a model has been derived which relates the ICR, wind speed, and ice σ^0 to a measured σ^0.

5.1.2 Prior Probability of Ice Generation

In order to calculate the ICR, a prior probability of sea ice is required which is generated by averaging daily RL ice maps. I have used the metric from Section 4.2.1 to determine the effect of different time wind lengths in the prior. Out of those tested, A 23 day prior minimizes the relative error in the Antarctic and is used in ICR processing. Quantitative results from these tests are available in Appendix B.

5.1.3 Polar Ice/Ocean Observation Distributions

To calculate the ICR, I computed monthly observation probability distributions for multiple years of QuikSCAT data over ice and ocean. These distributions are four dimensional for the measurement types: Vpol fore and aft, and Hpol fore and aft. These distributions are the probabilities of taking specific σ^0 measurements given that the measurement are taken over sea ice or ocean.

5.1.4 Posterior Probability of Ice Maps

Using the prior and observation probabilities, I calculate the posterior probability of sea ice. This image acts as a map of how likely it is for any given WVC to contain sea ice. This product detects polynias as well as disjoint ice and could be thresholded to make a single pass ice detection product. In this algorithm, the posterior is used to calculate the

ICR which is the spatial average of the posterior weighted by the spatial response function over the footprint.

5.1.5 Monte Carlo Ice-contamination Simulations

Monte Carlo simulations have been conducted to find the RMS error for different sets of ICR, wind speed, ice σ^0, and cross track location. These RMS errors have resulted in an ICR threshold look-up table which is used to discard contaminated σ^0 measurements. As wind speeds increase, ICR thresholds also increase meaning that more ice can be allowed in a measurement. As ice σ^0 increases, ICR thresholds decrease thereby prohibiting more ice in the measurement.

5.1.6 Metric Validation

Two metrics have been defined to validate ICR processing. The SOD measures the distance from the sea ice that winds can be retrieved, while the relative error measures how much extra error is caused by remaining ice. Methods for measuring these quantities have also been developed for which the SOD is on average 38.4 km smaller than the L2B for the Antarctic, and 15.9 km smaller in the Arctic. The relative error, using NCEP for comparison, also decreases in every case, which further validates the algorithm.

5.1.7 ICR Processed Wind Products

The ICR algorithm has been used to generate wind products for hundreds of revolutions in 2000 and 2004 and thousands of revolutions in 2008. These products contain both Arctic and Antarctic regions and can be used for climate studies.

5.1.8 Wind Histogram Validation

Wind histograms have been generated for 2008 data in order to compare and contrast agreement and disagreement in L2B and ICR processed winds. Histograms composed of WVCs for which L2B and ICR processing retrieved winds are used as ice-free histograms.

Histograms for which ICR retrieves winds and L2B does not retrieve winds agree stupendously with the ice-free case which shows that ICR winds are also uncontaminated. Histograms for which L2B retrieves winds and ICR does not retrieve winds has a histogram that is extremely biased from the ice-free case which shows that the discarded measurements were contaminated. Therefore the algorithm is validated using wind distributions.

5.2 Future Research

There are a number of areas of follow-on research. These areas include ideas for algorithm improvement, further validation studies, geophysical studies, and additional applications. These are listed in the following sections:

5.2.1 Experimentation with Priors

The ICR algorithm can be tested using other methods of prior generation. For example, one could observe how much ice moves from day to day and calculate a corresponding bandwidth which could be used in a spatial filter to smooth the current priors. Another possibility is to use a uniform prior to calculate the posterior which is then used as the prior in a second iteration. Additionally a causal prior could be developed in order to use ICR processing in real-time processing.

5.2.2 Measurement Deficiency Performance Analysis

ICR processing has the side effect of having fewer measurements that contribute to WVCs near the ice edge. Analysis can be done on how wind retrieval statistics are effected by this deficiency of measurements.

Although this thesis has developed ICR processing for the entire swath, the validation has only been performed on the inner swath. Similar analysis could be applied to the outer swath where fewer measurements are present.

5.2.3 Ambiguity Selection Investigation

Wind retrieval results in four or fewer ambiguities (multiple possible solutions). Generally these ambiguities are similar in magnitude and dissimilar in direction. The current

method of selecting the ambiguity is to use the wind which most closely matches L2B wind. However, ICR wind retrieval is not always performed near L2B winds. Methods for ambiguity selection for these cases should be investigated.

5.2.4 Wind Speed Dependent Relative Error

In the ICR algorithm, a 10% relative error threshold is applied for high wind speeds. However, for low wind speeds a threshold of 2 m/s RMS error is applied. In this thesis an overall relative error has been measured, but a wind speed dependent relative error could be used.

5.2.5 Polar Ocean Wind Studies

This thesis directly enables future studies of polar ocean winds. It may be feasible to study Katabatic winds that blow off the Antarctic continent. Another intriguing study is that of interactions between ocean winds and sea ice formation. Furthermore, the longevity of the QuikSCAT mission enables temporally long studies of polar wind trends. Such winds can also be applied to global climate models.

5.2.6 Implement for Iceberg Studies

Wind is important to understanding iceberg movement. Iceberg contamination is not explicitly mitigated using the current algorithm. However, a simple technique could extend ICR processing to do this. Currently, BYU tracks icebergs and keeps a record of their coordinates. In creating the prior, a constant probability of ice can be applied to a small region around the iceberg. Then a posterior can be calculated for the region using the sea-ice observation probabilities. This can enable the ICR to be calculated for the iceberg region.

5.2.7 Implementation for the Oceansat-2 Scatterometer

To continue polar wind coverage, ICR processing can be applied to the Oceansat-2 Scatterometer (OSCAT) [4], which is currently operational (as of March 15, 2012). The

OSCAT mission began on November 4, 2009, just as QuikSCAT ended its mission. Designed similarly to QuikSCAT, OSCAT utilizes a rotating pencil beam antenna system with horizontally and vertically polarizated beams.

The OSCAT spatial response function is not currently known. Since ICR processing requires the function, it must be estimated prior to implementing the ICR algorithm for OSCAT.

The algorithm's histograms and priors require sea-ice extent maps. Fortunately, BYU already produces OSCAT RL ice maps.

5.2.8 Implementation for the Advanced Scatterometer

The algorithm potentially can be applied to the Advanced Scatterometer (ASCAT). ASCAT was launched aboard the Metop-2 satellite in 2006 and is currently operational (as of March 15, 2012). ASCAT operates using 6 vertically polarized fan-beam antennas with 3 on each side of its track.

Like that of OSCAT, ASCAT's spatial response function must be estimated. The algorithm must be adapted to use a different set of observation types. For QuikSCAT four observations types are used: v-pol fore and aft, and h-pol for and aft. ASCAT only has v-pol measurements and additionally has an incidence angle dependence across the swath.

Bibliography

[1] M. Owen and D. Long, "Land-contamination compensation for QuikSCAT near-coastal wind retrieval," *Geoscience and Remote Sensing, IEEE Transactions on*, vol. 47, no. 3, pp. 839–850, 2009. 2, 14, 24, 25

[2] M. Jeffries and A. G. Union, *Antarctic sea ice: physical processes, interactions, and variability.* American Geophysical Union, 1998. 2, 14

[3] J. Allen and D. Long, "Microwave observations of daily Antarctic sea-ice edge expansion and contraction rates," *Geoscience and Remote Sensing Letters, IEEE*, vol. 3, no. 1, pp. 54 – 58, jan. 2006. 2, 14

[4] K. Padia and SCAT-DP Team, *Oceansat-2 scatterometer algorithms for sigma-0, processing and products format*, Advanced Image Processing Group, Signal and Image Processing Area, Space Applications Centre, Gujarat, India, 2010. 6, 49

[5] M. Spencer, C. Wu, and D. Long, "Improved resolution backscatter measurements with the SeaWinds pencil-beam scatterometer," *Geoscience and Remote Sensing, IEEE Transactions on*, vol. 38, no. 1, pp. 89 – 104, jan 2000. 6, 8

[6] I. Ashcraft and D. Long, "The spatial response function of seawinds backscatter measurements," in *Proceedings of SPIE*, vol. 5151, 2003, pp. 609–618. 7, 8

[7] T. Lungu and P. Callahan, "Quikscat science data product user̆2019s manual: Overview and geophysical data products," *D-18053-Rev A, version*, vol. 3, p. 91, 2006. 7, 10, 12

[8] D. Long, "High resolution wind retrieval from SeaWinds," in *Geoscience and Remote Sensing Symposium, 2002. IGARSS'02. 2002 IEEE International*, vol. 2. IEEE, 2002, pp. 751–753. 8

[9] B. Williams, M. Owen, and D. Long, "The ultra high resolution QuikSCAT product," in *Radar Conference, 2009 IEEE*. IEEE, 2009, pp. 1–6. 8, 12

[10] D. Long, P. Hardin, and P. Whiting, "Resolution enhancement of spaceborne scatterometer data," *Geoscience and Remote Sensing, IEEE Transactions on*, vol. 31, no. 3, pp. 700–715, 1993. 9

[11] D. Early and D. Long, "Image reconstruction and enhanced resolution imaging from irregular samples," *Geoscience and Remote Sensing, IEEE Transactions on*, vol. 39, no. 2, pp. 291–302, 2001. 9

[12] Q. Remund and D. Long, "Sea ice mapping algorithm for QuikScat and SeaWinds," in *Geoscience and Remote Sensing Symposium Proceedings, 1998. IGARSS'98. 1998 IEEE International*, vol. 3.   IEEE, 1998, pp. 1686–1688. 10

[13] ——, "Iterative estimation of Antarctic sea ice extent using SeaWinds data," in *Geoscience and Remote Sensing Symposium, 2000. Proceedings. IGARSS 2000. IEEE 2000 International*, vol. 2.   IEEE, 2000, pp. 491–493. 10

[14] M. Freilich and R. Dunbar, "Derivation of satellite wind model functions using operational surface wind analyses: An altimeter example," *Journal of geophysical research*, vol. 98, no. C8, pp. 14 633–14, 1993. 10

[15] F. Wentz and D. Smith, "A model function for the ocean-normalized radar cross section at 14 GHz derived from NSCAT observations," *Journal of geophysical research*, vol. 104, no. C5, pp. 11 499–11 514, 1999. 10

[16] F. Naderi, M. Freilich, and D. Long, "Spaceborne radar measurement of wind velocity over the ocean–an overview of the NSCAT scatterometer system," *Proceedings of the IEEE*, vol. 79, no. 6, pp. 850–866, 2002. 10

[17] C. Chi and F. Li, "A comparative study of several wind estimation algorithms for spaceborne scatterometers," *Geoscience and Remote Sensing, IEEE Transactions on*, vol. 26, no. 2, pp. 115–121, 1988. 12

[18] A. Stoffelen and M. Portabella, "On Bayesian scatterometer wind inversion," *Geoscience and Remote Sensing, IEEE Transactions on*, vol. 44, no. 6, pp. 1523–1533, 2006. 12

[19] T. E. Oliphant, "New techniques for wind scatterometery," Master's thesis, Brigham Young University, 1996. 12

[20] S. J. Shaffer, R. S. Dunbar, S. V. Hsiao, and D. G. Long, "A median-filter-based ambiguity removal algorithm for NSCAT," *IEEE Trans. Geosci. Remote Sens.*, vol. 29, no. 1, January 1991. 12

[21] D. W. Draper and D. G. Long, "An advanced ambiguity selection algorithm for SeaWinds," *IEEE Trans. Geosci. Remote Sens.*, vol. 41, no. 3, March 2003. 12

[22] *SeaWinds on ADEOS-II Level 2B Ocean Wind Vectors in 25km Swath*, Physical Oceanography DAAC, Jet Propulsion Laboratory, October 2002. 27

[23] "National centers for environmental predition," Mar 2011. [Online]. Available: http://www.ncep.noaa.gov/ 37

Appendix A

List of Acronyms

ASCAT - Advanced Scatterometer
GMF - Geophysical Model Function
HR - High Resolution
ICR - Ice Contribution Ratio
JPL - Jet Propulsion Laboratory
L2B - JPL 25 km Resolution Wind Product
NCEP - National Center for Environmental Prediction
OSCAT - Oceansat-2 Scatterometer
PMF - Probability Mass Function
RL - Remund-Long - algorithm for sea ice detection
RMS - Root-Mean-Squared
SIR - Scatterometer Image Reconstruction
SOD - Standoff distance
WVC - Wind Vector Cell
QMOD4 - GMF developed for QuikSCAT to better represent low and high wind
QuikSCAT - Quick Scatterometer

Appendix B

Performance Analysis for Various Priors

The ICR algorithm is implemented with a prior that is generated by averaging daily sea-ice maps taken from both previous and subsequent days in a time window. Here, the SOD and relative RMS error $\epsilon_{\rm rel}$ as defined in Section 4.2.1 are used to measure how different time windows affects algorithm performance. The metrics are measured for both HR and conventional ICR processed winds using 5, 11, 17, and 23 day time windows. The sets on which the metrics are measured are the Antarctic and Arctic oceans for 2000 and 2004 and the L2B product for comparison. The SOD and $\epsilon_{\rm rel}$ for each prior time window are displayed in Table B.1 and Table B.2 respectively. In each table, the metric is displayed for the 2.5 km HR and 25 km conventional products with the addition of the 25 km L2B product for comparison. The metrics are measured using 886 orbit revolutions. The Conventional ICR and L2B products combine more than 100,000 WVCs to measure the SOD, while HR ICR SOD uses approximately 0.5 million WVCs. Conventional ICR and L2B products combine more than 100,000 WVCs to measure $\epsilon_{\rm rel}$, while HR ICR $\epsilon_{\rm rel}$ uses approximately 1 million WVCs. For the L2B case, 3 revolutions are excluded because of severe and obvious ice contamination enabling a fairer comparison between the relative errors. Note that the Arctic results are obtained using the Antarctic observation probabilities. Performance could be improved by using Arctic observation probabilities for the Arctic region rather than the Antarctic.

Notice that in Table B.1 that the SOD goes up very consistently as the number of days in the prior increases. This may be attributed to a spatially larger transition band from low to high probability of ice due to more ice change that occurs within a larger time window. However, the standard deviation of the SOD for any given set and resolution is not much greater than 1 km. This demonstrates algorithm robustness in that the SOD is relatively insensitive to the prior. With a 23 day prior, the Antarctic SOD, averaged over 2000 and 2004, is 38.4 km lower than the L2B product's SOD. This means that winds are retrieved 38.4 km closer to the ice edge using ICR processing compared to the L2B product. ICR processing retrieves Arctic winds 16.0 km closer to the ice compared to the L2B product.

Table B.2 demonstrates that Antarctic $\epsilon_{\rm rel}$ decreases consistently as time window increases. This makes sense because one would expect the error to decrease as the distance from the ice increases as demonstrated in Table B.1. However, the Arctic $\epsilon_{\rm rel}$ increases as the time window increases. Still, the standard deviations of the Arctic winds across the 4 time windows are under 1.6%. In all cases the relative error is much less than the L2B product. The ICR retrieved winds demonstrated throughout this thesis are generated using a 23 day prior which has the minimum $\epsilon_{\rm rel}$ for the Antarctic out of the 4 time windows considered.

Table B.1:

SOD in km for ICR processed winds next to the ice edge using various lengths of time windows to generate the prior.

Res.	Set	5 day	11 day	17 day	23 day	L2B
2.5 km	Antarctic 2000	20.1	21.5	22.3	22.7	-
	Antarctic 2004	19.7	21.1	22.3	22.9	-
	Arctic 2000	19.6	21.0	21.6	22.1	-
	Arctic 2004	20.1	21.0	21.8	22.0	-
25 km	Antarctic 2000	20.5	21.9	22.6	22.8	57.9
	Antarctic 2004	20.4	21.5	22.7	23.1	64.7
	Arctic 2000	19.9	21.1	21.6	22.2	38.7
	Arctic 2004	19.9	20.9	21.7	21.8	37.2

Table B.2:

Relative RMS error ϵ_{rel} in % for ICR processed winds next to the ice edge using various lengths of time windows to generate the prior.

Res.	Set	5 day	11 day	17 day	23 day	L2B
2.5 km	Antarctic 2000	27.1	26.0	24.7	23.7	-
	Antarctic 2004	36.9	34.0	31.4	30.4	-
	Arctic 2000	15.1	15.3	15.6	16.5	-
	Arctic 2004	21.7	22.6	21.8	21.9	-
25 km	Antarctic 2000	19.7	18.1	18.4	18.1	31.6
	Antarctic 2004	30.0	30.0	27.5	27.3	34.3
	Arctic 2000	17.3	17.3	19.0	20.6	31.2
	Arctic 2004	24.6	24.8	25.2	26.7	40.0